MASTER IN ASTROPHYSICS AND SPACE SCIENCE

Erasmus Mundus Master
in Astrophysics and Space Science

Master's Thesis

Fermi Gamma-Ray Bursts: Precursors and Spectral lag

Supervisors:

Dr. Nelson Christensen
ARTEMIS, Observatoire Côte d'Azur

Dr. Eleonora Troja
University of Rome "Tor Vergata"

Author:

Ridha Fathima Mohideen Malik

Academic Year 2023/2024

This master's thesis is submitted in partial fulfillment of the requirements as part of the multiple degree, "Master Physique Fondamentale et Applications", awarded in the framework of the Erasmus Mundus Joint Master in Astrophysics and Space Science – MASS jointly delivered by a Consortium of four Universities: Tor Vergata University of Rome, University of Belgrade, University of Bremen, and Université Cote d'Azur, regulated by the MASS Consortium Agreement and funded by the EU under the call ERASMUS-EDU-2021-PEX-EMJM-MOB.

Contents

Abstract

Gamma-ray bursts (GRBs) are among the most luminous transients in the universe, detected daily by space telescopes like *Fermi* and *Swift*. Despite their abundance, no unified model explains their observed diversity. This thesis aims to understand GRB emission and classification in the era of multi-messenger astronomy. The work is divided into two parts. First, we focus on the search for γ-ray counterparts to gravitational-wave events. Specifically, we investigate the possibility of γ-ray emission coincident with or preceding compact binary mergers. We search for *Fermi* γ-ray precursors, extending the methodology of Stachie et al. (2022), to LIGO-*Virgo*-KAGRA (LVK) O4 merger candidates. Such a multi-messenger detection, if found, could provide insights into the physics of merger, and will also have implications for fundamental physics and cosmology. We report no significant candidates. In the second part, we shift our focus to explore the properties of the GRB prompt emission. Traditionally, GRBs were classified based on duration, with short GRBs associated with compact binary mergers, and long GRBs with massive star collapses. However, discoveries like GRB 060614 have challenged this paradigm. One of the potential parameters for a new GRB classification scheme is the spectral lag, which is the time lag seen between pulses of different energy (Gehrels et al., 2006). Spectral lag can also be employed towards the standardisation of GRBs as cosmological sirens (Norris et al., 2000). We developed a Python-based tool to provide rapid and well-constrained spectral lag estimations, primarily for *Fermi*-GBM GRBs. The tool uses a cross-correlation approach and bootstrapping for uncertainty estimation. We present the results of a sample of *Fermi* GRBs and compare it to the literature. The spectral lag estimation tool, when made publicly accessible, will aid in the rapid classification of GRBs, allowing timely follow-up of GRB events.

Chapter 1

Introduction

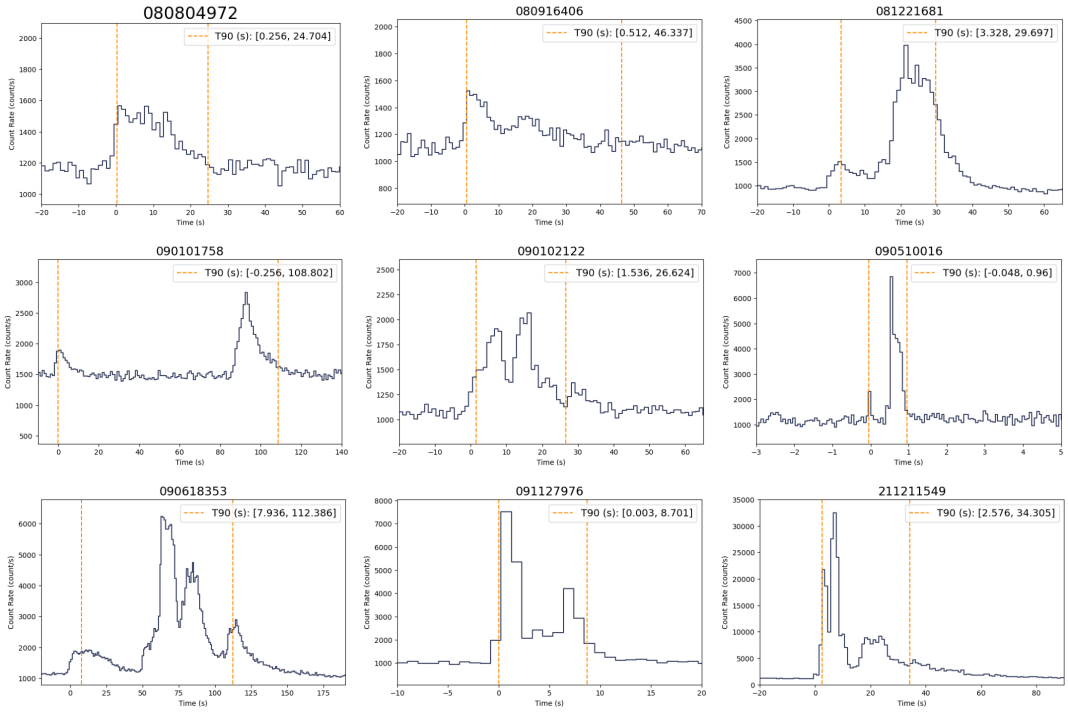

Figure 1.1: *"If you have seen one GRB, you've seen one GRB"*.
A sample of Fermi-GBM GRBs illustrating the diversity of lightcurves.

The intense γ-flashes detected by the *Vela* satellites in 1967, were soon pinned down to be of astrophysical origin. This class of luminous transients, called gamma-ray bursts (GRBs), signal the end of stellar life. In this cataclysmic event, energy exceeding 10^{53} ergs s^{-1} is released, and is observed in multiple electromagnetic (EM) bands. GRBs occur through two channels: the merger of neutron stars (NSs) and the collapse of a massive star. The resultant blackhole (BH) or magnetar, and its relativistic jet drive the emission. According to the fireball model, the internal energy conversions in the relativistic flow produce the intense prompt emission in γ-rays (Rees & Meszaros, 1994), and the external shock produced when the jet interacts with interstellar medium (ISM) powers the multi-wavelength afterglow (Mészáros & Rees, 1997). GRBs are also multi-messengers that emit gravitational waves (Abbott et al., 2017a) and predicted to emit neutrinos (Mészáros et al., 2004). Though the emission process is similar, the duration varies between mergers and collapsars. Canonically, using T_{90} which is the duration within which 90% of fluence is contained, mergers are found to give rise to GRBs with $T_{90} < 2$ s, and collapsars produce longer GRBs, with T_{90} spanning two seconds to a few hundred seconds, and rarely close to thousand seconds. This is visualised as the bimodal distribution of T_{90} (Kouveliotou et al., 1993), shown in Figure 1.2. Long GRBs are associated with supernovae (SNe) and star-forming regions, while short GRBs are associated with kilonovae (KNe) (Katz & Canel, 1996). This further implies a host galaxy association, where SGRBs should be found in early-type galaxies, whereas LGRBs in young star-forming galaxies.

The association of short GRBs to mergers was confirmed by the multi-messenger detection of GW170817 (Abbott et al., 2017a). The detection of GRB170817A 1.7 seconds after the GW170817 merger event, prompts the question if the delay is an inherent property of the emission, and if there are mechanisms that could produce γ-ray emission coincident or close to the merger. Chapter 2 provides a brief introduction to GRB emission and phenomenology, and the *Fermi* telescope. In Chapter 3, we try to understand the dynamics of emission from a binary system and what are the mechanisms at play close to the merger that can produce a de-

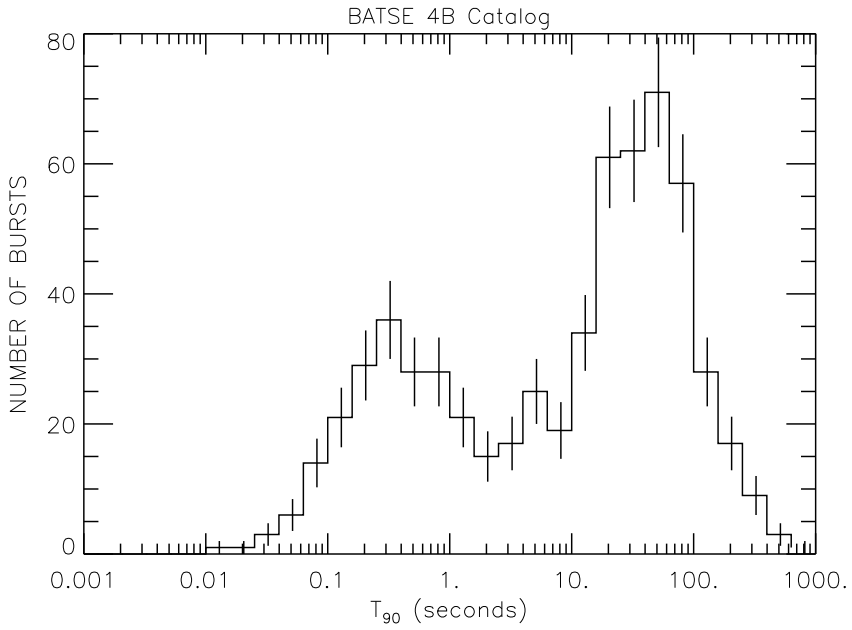

Figure 1.2: Bimodal distribution of T90 in BATSE Fourth Catalog (Paciesas et al., 1999)

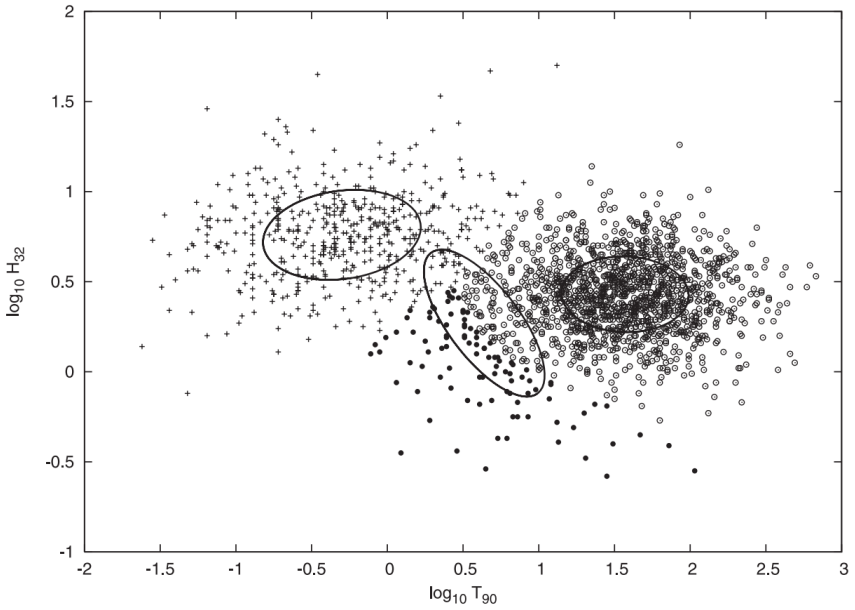

Figure 1.3: Hardness ratio vs T_90 for BATSE GRBs. The circles identify 3 groups in the classification (Horváth et al., 2006)

tectable signal. We extend this knowledge and employ the methodology of Stachie et al. (2022) to search for such precursor emissions.

In Figure 1.2, it should be noted that the T_{90} classification does not form clear binary classes. As it was made evident by the discovery of GRB 060605 and GRB 060614 by *Swift* (Gehrels et al., 2006), there indeed exists an 'intermediate' class of GRBs. T_{90} classification also depends on the instrument, the trigger criteria, and the detector physics. According to the collapsar model of Bromberg et al. (2013), 40% *Swift* and 15% *Fermi* SGRBs could be failed collapsars, while the BATSE ones are unaffected. This prompts us to look for new classification schemes based on other parameters, such as the hardness–ratio of total fluence in high-energy bands to that of low-energy bands–of the burst (Figure 1.3), peak luminosity, and spectral lag. In this context, our work focuses on providing a robust estimation of spectral lag, particularly for *Fermi* GRBs. We adapted the methodology of Norris et al. (2000) to estimate lags. We present the results of our simulations and an 'intermediate' case, GRB 211211A, to demonstrate the reliability of the tool in Chapter 5.

Chapter 2

GRB theory and observations

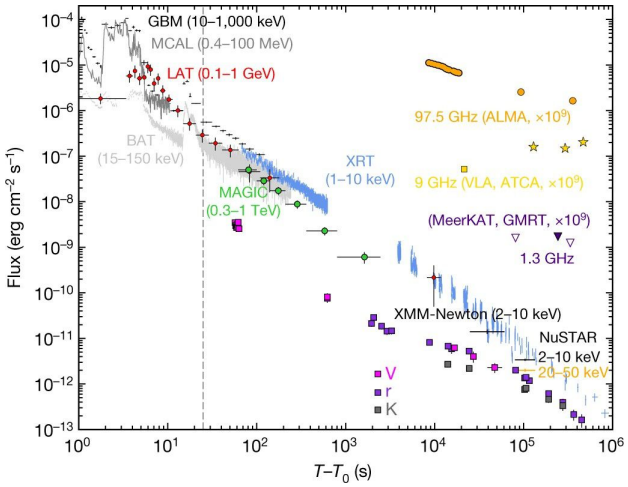

Figure 2.1: Multi-wavelength lightcurve of GRB 190114C
(MAGIC Collaboration et al., 2019)

GRBs have a diverse phenomenology arising from the complex and extreme physics at play. Many theoretical frameworks have been proposed over the years to explain the different phases of emission we observe. Figure 2.1 shows a multi-wavelength lightcurve of an LGRB, GRB 190114C. The primary γ-ray emission called the prompt, is followed by a decaying afterglow in X-ray, optical, and infrared up to radio. The SN or KN, if present, is observed superposed at late times

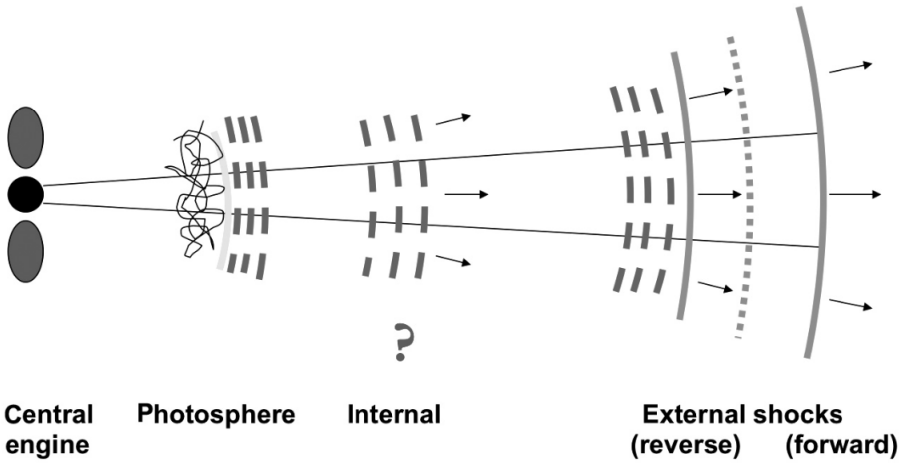

Figure 2.2: The fireball model illustrated by Wang et al. (2020)

of the optical-infrared afterglow. Additionally, some GRBs, like GRB 211211A, show a γ-ray precursor and extended emission. In this chapter, we will explore the key ingredients of the fireball model, the popular GRB emission model, in Section 2.1. Later, we will look at the spectral and temporal properties (Section 5.2 and 2.3) to understand the need for a robust method to estimate spectral lags (Section 2.3.1).

2.1 The fireball model

Paczynski (1986) and Goodman (1986) proposed the fireball model to explain the observed energetics of the GRBs (Figure 2.2). A fireball is an outflow of thick plasma from a highly energetic event, with initial energy larger than its rest mass. As it expands, the opacity decreases enough for γ-ray photons to escape. Rees and Mesazaros (1992; 1994; 1997) proposed that synchrotron emission occurs as a result of the shocks of the relativistic outflow. The interaction of shells of plasma within the relativistic outflow gives rise to the prompt, and the shocks produced when the shells hit the ISM give rise to the afterglow. The internal shock model

explains the rapid variability and non-thermal spectra observed in GRBs. The external shock model is supported by the observed smooth, long-duration afterglows observed.

2.2 Spectral properties

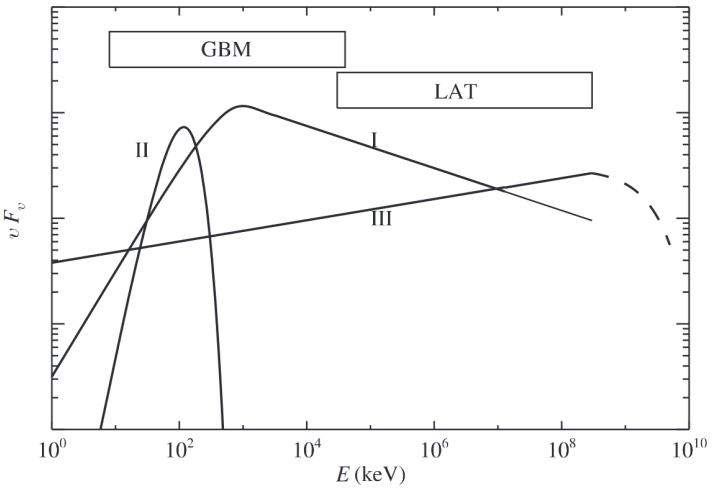

Figure 2.3: The three components of GRB spectrum (Zhang, 2018).
I refers to the non-thermal Band function. II is the thermal component. III is the mysterious component, probably involving inverse-Compton scattering. The boxes on the top highlight the coverage of the *Fermi* instruments.

Band et al. (1993) modelled the non-thermal spectra of GRB (Figure 2.3 as a broken power law joined smoothly at the break energy.

$$N(E) = \begin{cases} A \left(\frac{E}{100\ \mathrm{keV}}\right)^{\alpha} \exp\left(-\frac{E}{E_0}\right), & E \leq (\alpha-\beta)E_0 \\ A \left[\frac{(\alpha-\beta)E_0}{100\ \mathrm{keV}}\right]^{\alpha-\beta} \exp\left(\beta-\alpha\right) \left(\frac{E}{100\ \mathrm{keV}}\right)^{\beta}, & E > (\alpha-\beta)E_0, \end{cases} \tag{2.1}$$

where $N(E)$ is the photon flux (counts/sec/cm^2/keV), α is the low-energy spectral index, β is the high-energy spectral index, E_0 is the break energy and A is the normalization constant.

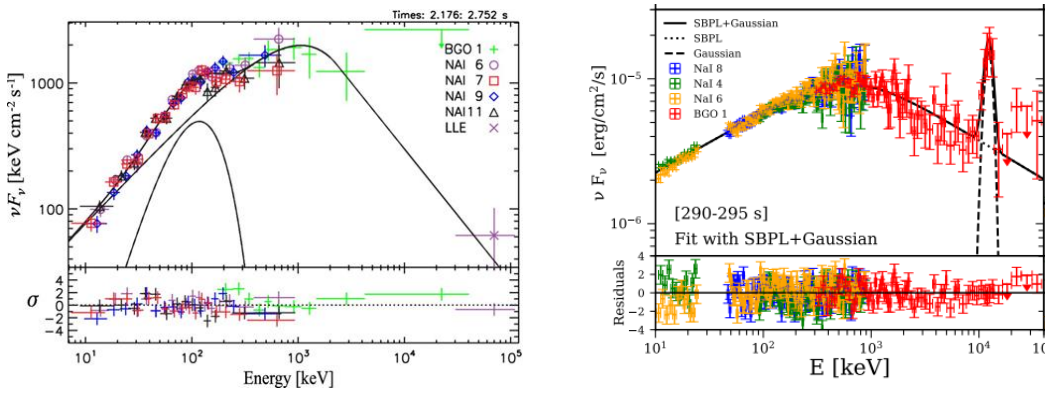

Figure 2.4: Spectral energy distributions (SED) of GRB 110721A with a thermal component (left, Iyyani et al. (2013)) and GRB 221009A with an emission line (right, Edvige Ravasio et al. (2023))

Since then, a thermal component has also been identified, attributed to photospheric emission in some GRBs, and a third component whose origin is still debated (Zhang, 2018). A recent work on GRB 221009A reported an emission line feature (Edvige Ravasio et al., 2023). GRB spectra evolve significantly over time, hardening or softening, and can vary with the progenitor. Traditionally, SGBRs are harder than LGRBs. Goldstein et al. (2016) proposed a model for the observed hard spectra of SGBRs as:

$$N(E) = \left(\frac{E}{E_0}\right)^{\alpha} \exp\left[-\frac{(\alpha+2)E}{E_{\text{peak}}}\right]. \tag{2.2}$$

But as with the T_{90} classification, this is not strictly followed by all GRBs. Hence, it becomes important to have parameters like spectral lags to understand the connection between spectral properties and GRB classes.

2.3 Prompt phenomenology

High-energy detectors in space like the *Swift* and the *Fermi* are triggered when the photon rates exceed the instrumental threshold. The following episode of peaked emission in sub-MeV energies is called the prompt. The pulse shapes vary widely between different GRB lightcurves (Figure 1.1). This suggests that stochastic processes in the central engine of GRBs govern the complex shapes we observe. Each irregular pulse could be considered as a superposition of multiple pulses (Norris et al., 1996). The pulse shapes also vary in different energy bands and their arrival is also not coincident. This delay in the arrival of the photons of different energies, known as spectral lag, was observed by Norris et al. (2000) in BATSE GRBs.

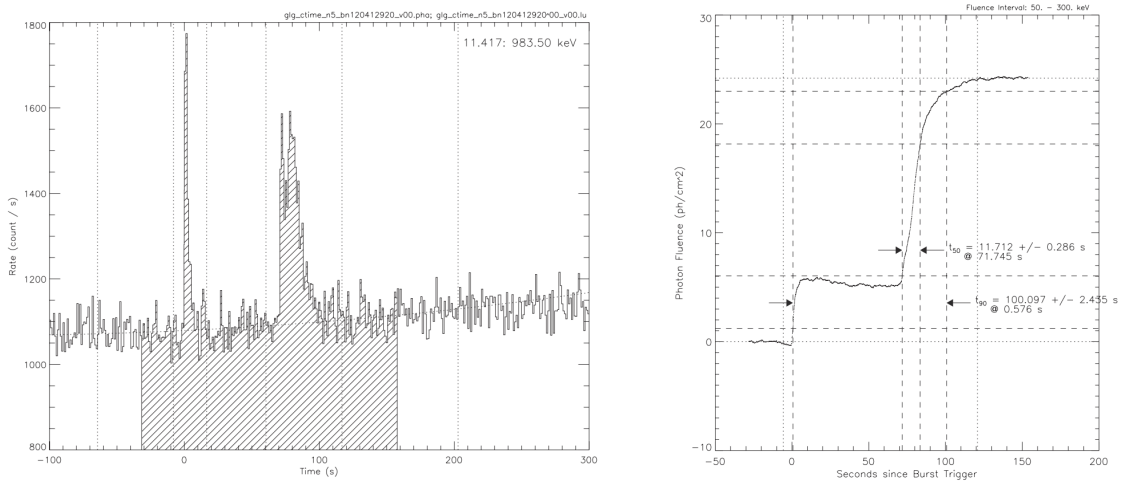

Figure 2.5: GRB 120412A lightcurve with T_{90} duration shaded (left) and the corresponding cut-offs on the cumulative curve (right) (von Kienlin et al., 2014)

2.3.1 Spectral lags

Spectral lags in GRBs, the delay of low-energy photons relative to high-energy photons, provide valuable insights into GRB emission mechanisms and physical properties. It is easy to imagine this as a consequence of spectral evolution during pulse decay (Dermer, 1998; Kocevski & Liang, 2003). As the peak of the spectrum shifts to lower energy, it manifests as a delayed arrival of low-energy temporal pulses (Figure 2.6). Another explanation involves the geometry of the fireball emission. High-energy photons are produced earlier in the expansion of the fireball compared to low-energy photons, and therefore high-energy photons have to travel less distance than low-energy photons to reach the observer (Figure 2.7). This kinematic effect could produce the observed lag (Salmonson, 2000; Ioka & Nakamura, 2001). Furthermore, cosmological redshift stretches time intervals between photon arrivals in distant GRBs, enhancing observed lags (Ukwatta et al., 2012).

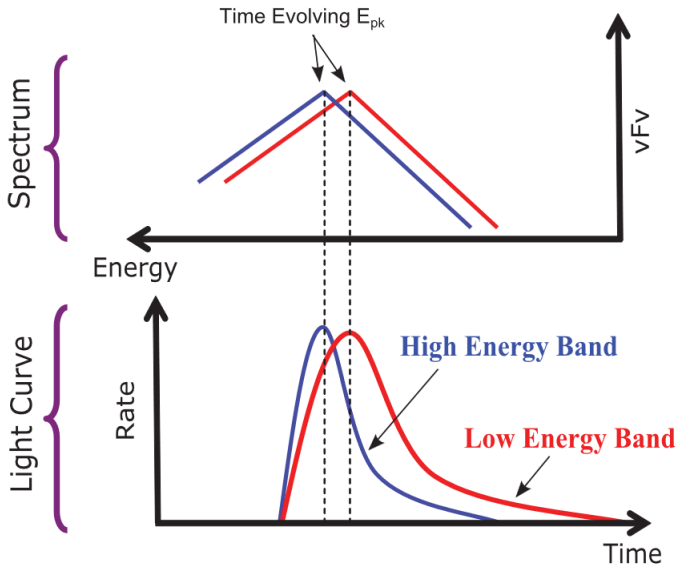

Figure 2.6: Illustration of lag due to spectral evolution (Ukwatta et al., 2012).

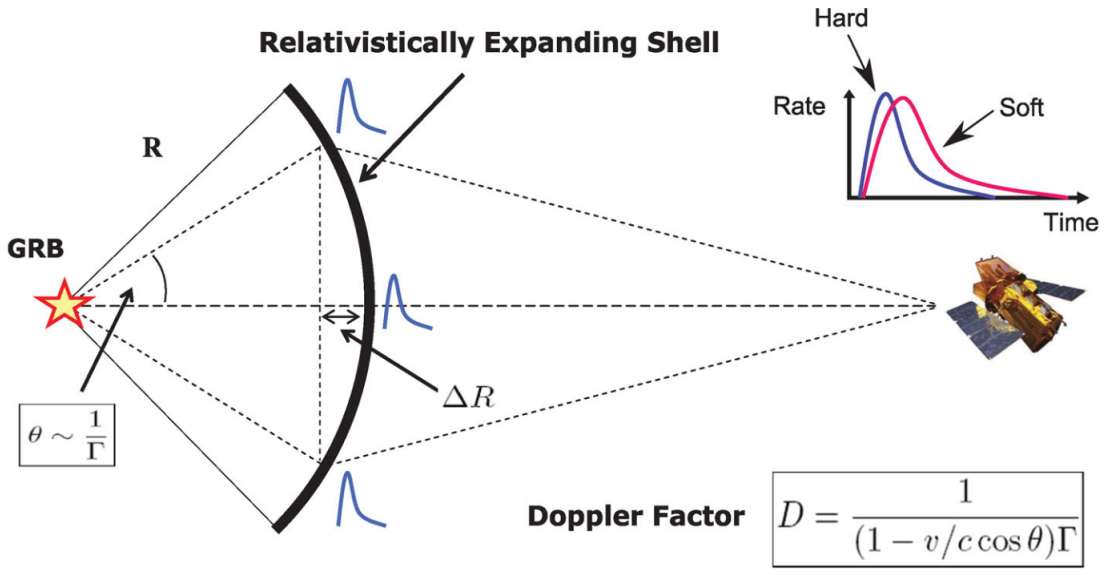

Figure 2.7: Illustration of lag due to curvature effect (Ukwatta et al., 2012).

Typically, these lags are positive (low-energy pulses are delayed with respect to high-energy pulses), and increase with energy separation. Additionally, a correlation exists between spectral lag and GRB luminosity (Norris et al., 2000), making spectral lags potential distance indicators. As noted by works such as Ukwatta et al. (2010) and Bernardini et al. (2015), the lags of SGRBs are smaller than LGRBs. SGRBs having shorter lags could be attributed to their compactness in the kinematic model of lags, while LGRBs' significant spectral evolution could explain the wider range of lags we observe. This distribution of spectral lags makes them an interesting diagnostic tool for GRB classification. In practice, such an application is limited by the challenges in constraining uncertainties and a lack of a unified approach. This work has attempted to solve this problem with the methodology of Norris et al. (2000), using the modular functionality of `Python`-programming language (Chapter 5).

2.4 Fermi-GBM

In the last two decades, the *Fermi* space telescope, together with *Swift* (Gehrels et al., 2004), has been at the forefront of developing our understanding of GRBs.*Fermi Gamma-ray Space Telescope* is on-board a low-Earth orbit (LEO) satellite at an altitude of $\sim$ 535 km altitude, and an inclination of 28.5*degree* with respect to the Earth's equator. It has a wide field view of $\sim$ 8 sr and observes in a wide energy range from 10 keV to 300 GeV, making it a crucial tool in multi-messenger astronomy. *Fermi* accomplishes this with its two instruments: Large Area Telescope (LAT, Atwood et al. (2009)) covering 20 MeV to 300 GeV, and Gamma-ray Burst Monitor (GBM, Meegan et al. (2009) operating in 8 keV to 40 MeV (Figure 2.8). This thesis uses *Fermi*-GBM data.

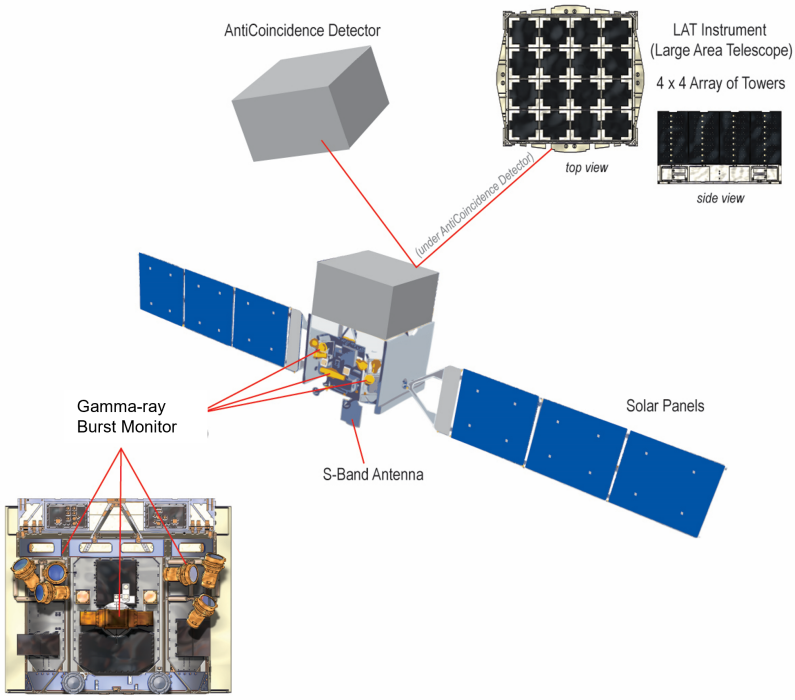

Figure 2.8: The Fermi satellite: the LAT instrument expanded on top-right and the GBM constellation in bottom-left. Credit: Lynn Cominsky/*Fermi* collaboration

Fermi-GBM is a constellation of twelve Sodium Iodide (NaI) and two Bismuth

Germanate (BGO) scintillators, covering 8 keV – 1 MeV and 150 keV – 40 MeV respectively. The scintillators interact with incoming γ-rays and produce low-energy photons. The data processing unit (DPU) of GBM amplifies the signal with a photon multiplier tube and digitalises it. The photon counts are accumulated at different time resolutions, time is tagged and packaged with detector information. GBM has a time resolution of 2μs. DPU also identifies triggers and computes localisation. To be classified as a trigger, *Fermi*-GBM requires at least two NaI detectors in $50 - 300$ keV to be 4.5σ above the background, on a 1.024s timescale. Depending on the observed background rate and conditions on-board, the trigger threshold of fluence varies. The DPU also localises the trigger and sends the information to the *Fermi* computer, which can then command the relocation of spacecraft if necessary. As of August 30, 2024, *Fermi* has detected over 3000 GRBs since its launch in 2008.

2.4.1 Data and time

Fermi packages its data as three types:

- **Time-tagged event (TTE)** is a time-energy object that provides unbinned photon counts in the native 2μs resolution and 128 energy channels.
- **Pulsar height analysis (PHA)** data type comes in two classes: **CTIME** is a time object with energy binned into 8 channels, and **CSPEC** is an energy object with time binned at 64 ms at the time of burst (256 ms normal operations).
- **Response (RSP)** contains the detector response matrix. Detectors never perform ideally and respond at the same rate. It's important to remember all detectors have limitations imposed by physics. For example, high-energy cosmic rays interacting with the NaI detectors create phosphorescence. Then there exists the effect of the spacecraft geometry and location with respect to the Sun and Moon, major local γ-ray sources.

Fermi uses the Global Positioning System (GPS) time for navigation and the Mission-Ellapsed Time (MET) system for observations to avoid errors from leap second additions used in the Terrestrial Time (TT) system. MET corresponds to the number of seconds elapsed since January 1, 2001, 00:00:00 UTC.

2.4.2 Noise sources

Despite the corrections taken, there are many other noise sources that can occur from clock glitches and calibration uncertainties to space weather interference. These are elaborated on the High-Energy Astrophysics Science Archive Research Center (HEASARC) site [1].

An important noise source, relevant to the search described in Chapter 4, is the South Atlantic Anomaly (SAA), which can be described as a "dent" in the Earth's magnetosphere. This weakness in the strength of the magnetic field allows for an influx of charged particles that exceed the flux of primary cosmic rays. In its 96-minute LEO, *Fermi* passes through this flux of charged particles, which affects the on-board instruments. Hence, in this duration, the satellite switches to a maintenance mode and returns to science operations after exiting this SAA, which is characterised by a 12-sided convex polygon (Abdo et al., 2009).

[1] https://fermi.gsfc.nasa.gov/ssc/data/analysis/caveats.html

Chapter 3

Gamma-ray precursors

GWs are an indispensable probe of the early phase of a GRB and their progenitors. Developing an integrated view of GW and GRB emission also helps us develop and constrain our astrophysical models, and also contributes to testing fundamental physics. In this chapter, we try to understand the physics of GW wave emission from compact binary coalescence (CBC). The relevant compact objects for this thesis are NSs and BHs. When referring to BHs, we are specifically talking about stellar-mass BHs.

3.1 GW radiation from binary systems

Consider a system of two compact objects in flat space-time, orbiting each other with an angular frequency, ω_s. In Newtonian approximation, we can treat them like point masses at a distance $\mathbf{R} = \mathbf{r_2} - \mathbf{r_1}$. Let us constrain the circular orbital motion to (x, y) plane given by,

$$x_0(t) = R\cos\left(\omega_s t + \frac{\pi}{2}\right)$$

$$y_0(t) = R\sin\left(\omega_s t + \frac{\pi}{2}\right)$$

$$z_0(t) = 0.$$

It is convenient to choose the reference frame centred at the centre of mass (CM) $\mathbf{r_{CM}} = (m_1\mathbf{r_1} + m_2\mathbf{r_2})/(m_1 + m_2) = 0$. The dynamics can now be described as that of a single body with a reduced mass $\mu = m_1 m_2/(m_1 + m_2)$ in a circular orbit. In the CM frame, the second mass moment is

$$M^{ij}(t) = \mu x_0^i(t) x_0^j(t). \tag{3.1}$$

For the chosen orbit, Equation 3.1 becomes,

$$M_{11} = \mu R^2 \frac{1 - \cos 2\omega_s t}{2},$$

$$M_{22} = \mu R^2 \frac{1 + \cos 2\omega_s t}{2},$$

$$M_{12} = \frac{1}{2}\mu R^2 \sin 2\omega_s t.$$

The quadrupole mass moment is then given by,

$$Q_{ij} = M_{ij} - \frac{1}{3}\delta_{ij} M_{kk}. \tag{3.2}$$

Once we have the moments, we can compute the angular distribution of the quadrupole GW emission as shown by Maggiore (2007). The strain produced is

$$h_+(t, \theta, \phi) = \frac{4G\mu\omega_s^2 R^2}{rc^4} \left(\frac{1 + \cos^2 i}{2}\right) \cos\left(2\omega_s t_{ret} + 2\phi\right), \tag{3.3}$$

$$h_\times(t, \theta, \phi) = \frac{4G\mu\omega_s^2 R^2}{rc^4} \cos\theta \sin\left(2\omega_s t_{ret} + 2\phi\right), \tag{3.4}$$

where:

- i is the angle between the normal to the orbit and the line of sight (LOS),
- r is the distance between the source and the observer,
- $t_{ret} = t - r/c$ is the retarded time and for a distant source $t_{ret} \sim t - r/c$,

- ϕ is a constant and can be eliminated.

The quadrupole radiation is emitted at $2\omega_s$ From the quadrupole formula, the radiated differential power is,

$$\frac{dP}{d\Omega} = \frac{G}{8\pi c^5}\left\langle \dddot{Q}_{ij}\dddot{Q}^{ij}\right\rangle = \frac{2G\mu^2 r^4\omega_s^6}{\pi c^5}g(i),$$

where, $g(i) = ((1+\cos^2 i)^2/4) + \cos^2 i$ contains information on the emission geometry and polarisation. The emission shape looks like a dumbbell, suppressed along the plane of the binary and beamed radially, similar to EM radiation. When $i = \pi/2$, an edge-on view, the waves are linearly polarised; When we see face-on, $i = 0$, the waves are circularly polarised; In between the extremes, the waves are elliptically polarised. The total power radiated is

$$P = \frac{32}{5}\frac{G\mu^2}{c^5}R^4\omega_s^6. \tag{3.5}$$

As GWs are emitted, the system loses orbital energy $E_{orbit} = -Gm_1m_2/2R$, and radius R decreases. According to Kepler's law $\omega_s = Gm/R^3$, the frequency of the rotation ω_s and the emitted waves $\omega_{GW} = \omega_s$ increases. As long as $\dot{\omega}_s << \omega_s^2$, we are in the so-called quasi-circular orbit approximation. Equalising P_{quad} to $-\dot{E}_{orbit}$, one can obtain

$$\dot{\omega}_{GW} = \frac{96}{5}\pi^{8/3}\left(\frac{G\mathcal{M}}{c^3}\right)^{5/3}\omega_{GW}^{11/3}. \tag{3.6}$$

Here, we have introduced the chirp mass:

$$\mathcal{M} = \frac{(m_1m_2)^{3/5}}{(m_1+m_2)^{1/5}}. \tag{3.7}$$

Integrating Equation 3.6, we get

$$\omega_{GW}(t) = \left(\frac{5}{256}\frac{1}{\tau}\right)^{3/8}\left(\frac{G\mathcal{M}}{c^3}\right)^{-5/8}, \tag{3.8}$$

where, $\tau = t_c - t$, and t_c is the time to coalescence. As the system nears coalescence, the quasi-stable orbit approximation is no longer valid, as the quadrupole

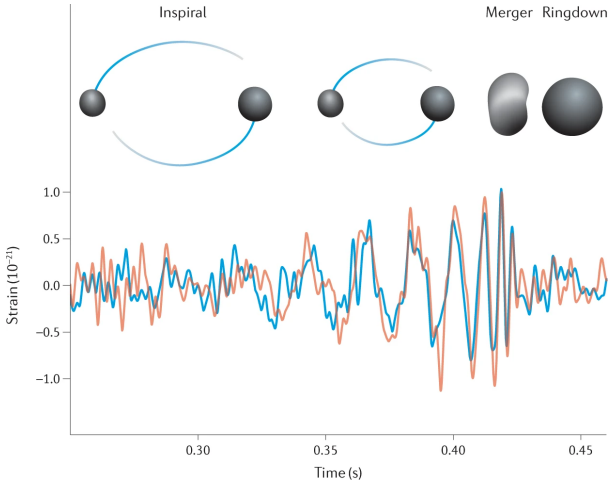

Figure 3.1: An illustration of different phases of compact binary merger against the LIGO-*Virgo* data of GW170817 (Bailes et al., 2021).

formalism fails as the separation is too small and cannot be treated as point masses if tidal effects rise. Note that in our derivation, we have assumed a flat spacetime in a weak-field regime. Then, we have to consider post-Newtonian formalism and numerical relativity. It is possible to define the innermost stable circular orbit (ISCO) of this adiabatic inspiral before it plunges and merges. From a fully relativistic computation, this minimum distance is found to be given by $r_{ISCO} = 6G(m_1 + m_2)/c^2$. This can be translated to frequency, and the quadrupolar radiation is emitted until a maximum frequency of $2f_{ISCO}$. For binary NSs (BNSs), of masses $1.4M_\odot$ each, $f_{ISCO} = 800$ Hz and for binary BHs (BBHs) of $10M_\odot$ each, $f_{ISCO} = 200$ Hz.

3.2 EM radiation from binary systems

Binary systems like pulsars—highly magnetised and rapidly rotating NSs with emission regions—could be observed in EM and we can study their orbital properties. In fact, such a study of a pulsar binary led to one of the earliest confirmations of General Relativity. In the infamous Hulse-Taylor pulsar system (Hulse

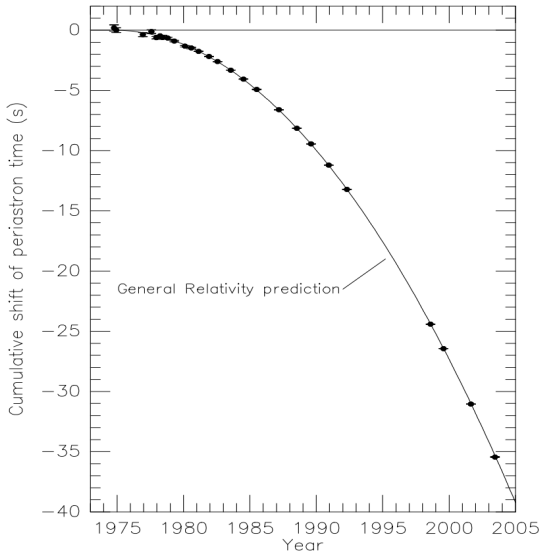

Figure 3.2: Cumulative decrease in periastron time over 30 years compared with General Relativity prediction (Weisberg & Taylor, 1984).

& Taylor, 1975), the orbital period was shown to decrease with time, observed as the time of periastron (closest approach) occurring earlier and earlier. Figure 3.2 shows how the data strictly follows the General Relativity prediction, providing indirect evidence of the existence of gravitational waves (Taylor et al., 1979). But oftentimes compact objects are EM-dark and only observed at their end stages after merger as GRBs or KNe. Several works have theorised possible emission channels to observe them before the merger. In this section, we explore the possibility of having such a "precursor".

To produce a precursor, at least one of the compact objects in the binary should be an NS[1], and a mechanism of emission from the NS before the merger. Some mechanisms proposed are the resonant shattering and the BH-battery model. In the first model, the resonant excitation of NS oscillation modes (i-modes, g-modes, f-modes) by the tidal interaction during inspiral causes the crust to fracture and

[1]While BBHs can produce emission if they possess accretion disks, we limit this thesis to NS systems.

release energy. The heating of NS of tidal compression at the late stages of merger could also cause crustal failure and premerger emissions. In the case of an NSBH binary, the BH companion should have a low mass and a high spin to disrupt the NS by this mechanism; otherwise, it will be swallowed whole.

In the BH-battery model proposed by McWilliams & Levin (2011), when the BH enters the magnetosphere of the NS, the magnetic field connects the BH horizon with the NS which acts as an external resistor, and the electron-positron plasma within the magnetosphere provides the current. The combination of the orbital motion and spin of the BH powers the circuit through Blandford & Znajek mechanism. The rotation of the BH twists the magnetic lines producing an electric field in the vicinity of the BH. Charged particles in the magnetosphere, in which the BH is embedded, are accelerated by this electric field producing synchrotron radiation, which is beamed by the dipole magnetic field of the NS. In this process, the BH loses spin and energy, and the resulting emission is observed as a precursor to the prompt GRB. The luminosity produced in this channel is also higher than resonant shattering. Since this model does not require tidal disruption, an emission from such a process would be more numerous than the previous scenario and could be detected by γ-ray telescopes like *Fermi* and *Swift*.

It is important to recall from Section 2.1 that, at high luminosities, opacity from pair-production produces a fireball. Schnittman et al. (2018) theorised that this emission from an NS in a binary will be modulated in its inspiral orbit. Two major processes that modulate the emission are gravitational lensing, as the BH bends the space-time, and relativistic beaming, concentrating the radiation in the direction of motion. The resulting lightcurve evolves with the GW emission and has a similar chirp form (Figure 3.3.

Precursors have been detected in *Swift* (Figure 3.4, Troja et al. (2010)) and *Fermi* observations (Zhu, 2015; Wang et al., 2020). While Li et al. (2021) observed that precursors lasted for shorter durations than the prompt, Wang et al. (2020) reported some GRBs with comparable durations. Timing and energetics of observed

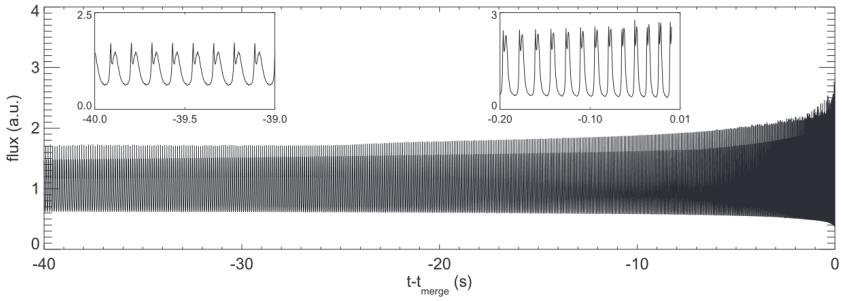

Figure 3.3: The EM "chirp" simulated by Schnittman et al. (2018)

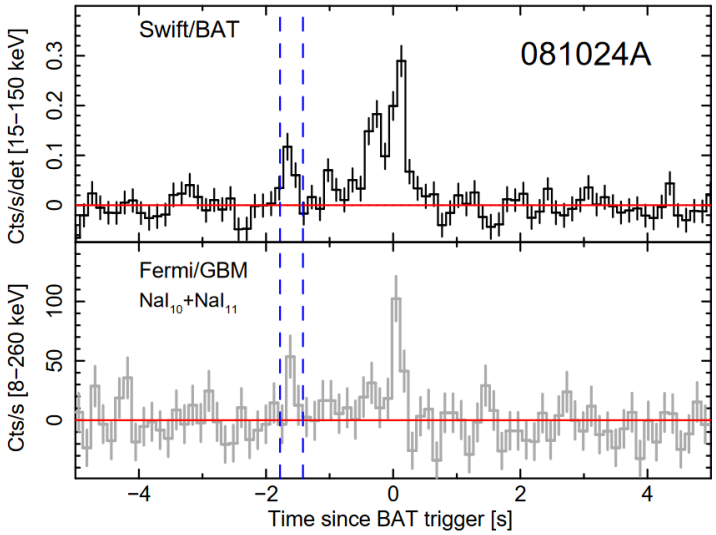

Figure 3.4: *Swift*-BAT mask-weighted lightcurves ($15 - 150$ keV) and *Fermi*-GBM lightcurves ($8 - 260$ keV) of short GRBs with possible precursor activity in GRB 081024A. Dashed blue vertical lines mark the precursor duration and the red horizontal line is the background.

precursors are consistent with resonant shattering models (Suvorov et al., 2024). Spectroscopic investigation of the precursors will reveal whether the underlying emission mechanism is thermal or arises from magnetic interaction. Polarimetric studies will give insights into the properties of the magnetic field of the NS. Thus, such observations will be instrumental in understanding the EOS of an NS.

Current γ-ray detectors lack the resolution and sensitivity to perform spectroscopy and polarisation in the brief, often faint precursor events. The recently launched SVOM mission (Wei et al., 2016) can improve this situation. Like *Swift*, SVOM can slew and point when a GRB is triggered, which could allow early observations of precursors. The broad energy range and improved sensitivity allows to characterise the spectral properties of both the softer precursors (Troja et al., 2010) and prompt emission. There are upcoming instruments like the POLAR-2 (Hulsman, 2020) to address the polarimetry problem.

3.3 Laser interferometers

In 1962, Gertsenshtein and Pustovoit proposed laser interferometers to achieve the sensitivity to detect GWs. In 1972, Weiss elaborated on this idea and envisioned what now has developed into the Laser Interferometer Gravitational-wave Observatory (LIGO). Figure 3.5 shows a Michelson interferometer set-up with Fabry-Perot cavities and power recycling. A highly-stabilised powerful laser beam is bifurcated into the two arms of the interferometer where it is reflected by mirrors at the end of the arms. The reflected light interferes and the signal is received at the read-out end. The mirrors are uniformly polished and coated with materials that reduce the instability of the laser from reflection and thermal noise. The Fabry-Perot cavities in the arms increase the effective optical path length. The mirrors are also isolated to prevent seismic vibrations. The entire set-up is built inside an ultra-high vacuum to minimize optical path fluctuations due to refractive index variations. Such extensive engineering has allowed LIGO to achieve the precision

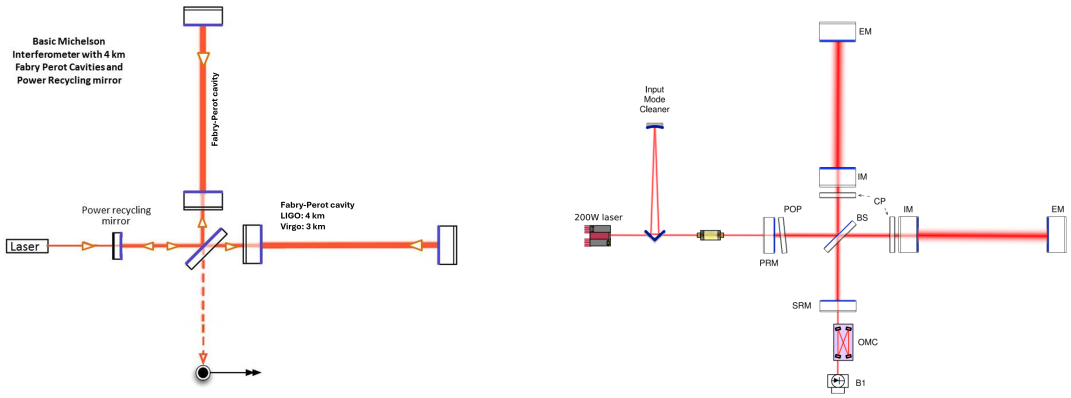

Figure 3.5: Left: Basic Michelson interferometer set-up (Credit: LIGO lab, Caltech). Right: A simplified optical layout of the Advanced *Virgo* (Credit: Acernese et al. (2015)). Each Fabry-Perot cavity is formed by an Input Mirror (IM) and an End Mirror (EM*). The recycling cavities at the centre of the interferometer are formed by the Power Recycling Mirror (PRM), the Signal Recycling Mirror (SRM), and the two IMs. (*EM refers to End Mirror only in this instance.)

required to measure the strain of space-time from gravitational waves. The strain changes the length of arms producing the signal and the waveform of the signal is analysed by comparing with theoretical models. The first detection of GWs in 2015 (Abbott et al., 2016) proved Einstein's General Relativity after a century.

Now, we have a network of GW detectors with advanced detectors pushing quantum limits of sensitivity. For example, Advanced *Virgo* has improved sensitivity by increasing laser power from 10W to 200W and upgrades to overcome quantum noise, thereby reducing shot noise limitations at high frequencies, larger test masses to reduce thermal noise contributions, and multi-stage pendulum suspensions with active and passive damping to attenuate seismic and thermal noise and introducing signal recycling to resonantly enhance the signal in targeted frequency ranges. The signal obtained from the interferometer is matched with theoretical models and parameters such as mass, spins, orientation, distance, and sky location are estimated with Bilby (Ashton et al., 2019) and Bayestar (Singer & Price, 2016). Currently, the LVK collaboration—made of the two Advanced LIGO

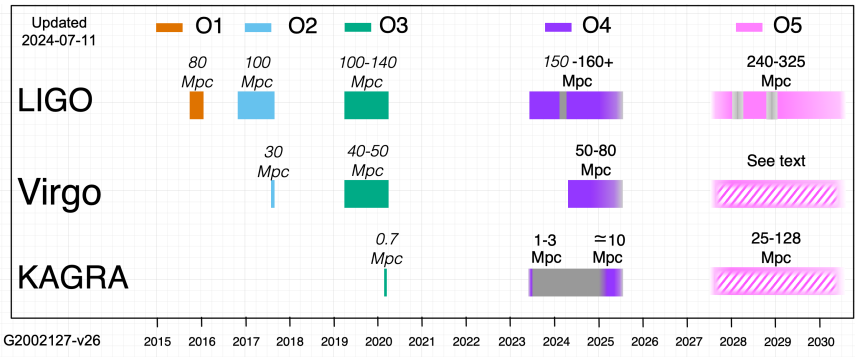

Figure 3.6: The distances refer to the detection limit for a BNS merger. Credits: LVK collaboration

detectors in Hanford and Livingston, USA, the Advanced *Virgo* detector in Italy, and the new KAGRA in Japan—is mid-way through the 4th observation run. Figure 3.6 shows the observation timeline and the detection limits for a BNS merger.

3.3.1 GW170817

On August 17, 2017, 12:41:04 UTC, the first compact BNS merger detection was by Advanced LIGO-Hanford and Livingston, and *Virgo*. The detection by all three online detectors at the time of observation implied astrophysical origin. With further noise analysis and reduction, the signal was estimated to have a signal-to-noise ratio, $SNR = 32.4$, and a false alarm rate, $FAR = 1.1 \times 10^{-6}$ Hz, equivalent to 1 in 100 years (Abbott et al., 2017a).

Following the GW event, a SGRB was detected 1.7 seconds later by *Fermi* (Goldstein et al., 2017) and confirmed by INTEGRAL (Savchenko et al., 2017). This event confirmed the merger and SGRB association. The arrival of GWs and γ-rays constrained the difference in their propagation speeds to within about one part in 10^{15}, providing a stringent test of General Relativity (Abbott et al., 2017c). Adding to the enormity of the breakthrough, the event was followed by detection of optical afterglow with a KN (Arcavi et al., 2017; Coulter et al., 2017; Lipunov

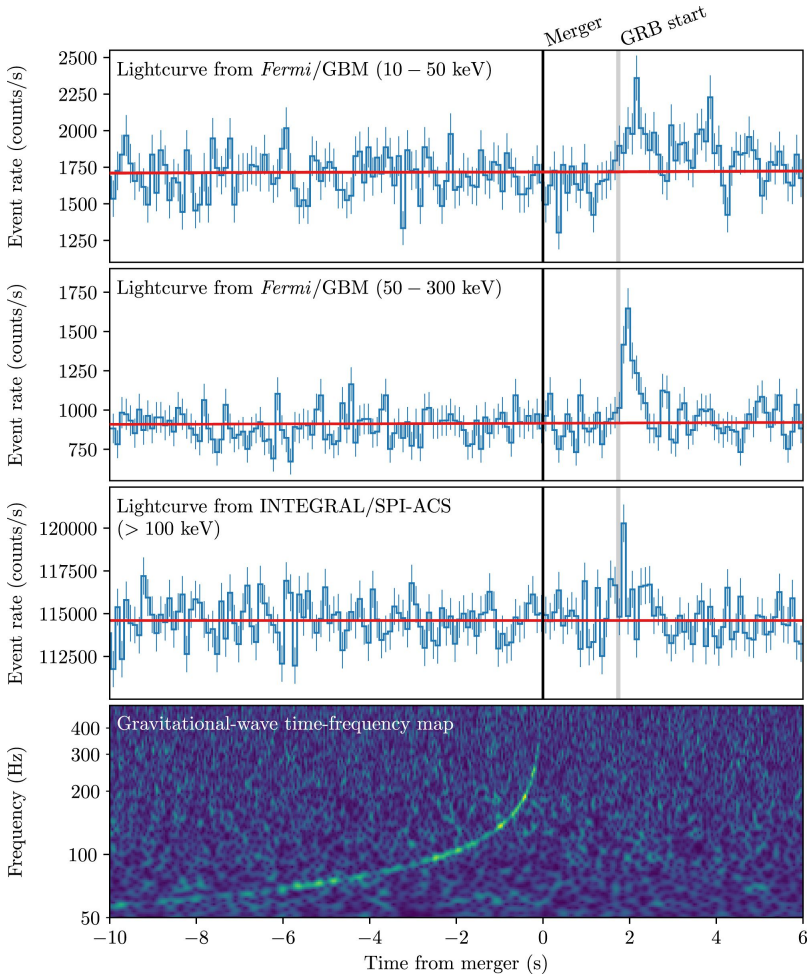

Figure 3.7: GW170817 and GRB170817A (Abbott et al., 2017c)

et al., 2017; Tanvir et al., 2017; Soares-Santos et al., 2017; Valenti et al., 2017), X-ray afterglow (Troja et al., 2017) and radio afterglow (Hallinan et al., 2017). The KN observations provided strong evidence for the production of r-process elements in BNS mergers. Combining GW with multi-wavelength EM observations allowed for detailed modelling of the merger's outflow, revealing that the jet was viewed off-axis (Mooley et al., 2018). This result breaks the degeneracy of inclination angle and luminosity distance. Furthermore, the host galaxy was localised to be an elliptical galaxy, NGC 4993, at 41.0 ± 3.1 Mpc enabling an independent measurement of the Hubble constant, demonstrating the potential of gravitational wave sources as cosmological sirens (Abbott et al., 2017b). Given the scientific output from a multi-messenger event like GW170817, there has been great interest in searching for the next event.

Chapter 4

Search for modulated gamma-ray precursors

In this chapter, we discuss the methodology for searching modulated γ-ray precursors as proposed by Stachie et al. (2022) (Hereafter, S22). Such a signal is best observed by *Fermi* due to the wide energy and spatial coverage. We extend the search of S22 NSBH candidates from the LVK-O4 run and discuss the results in Section 4.4.1.

4.1 LVK-O4 candidates

4.1.1 GW230529

Abac et al. (2024) was detected by LIGO-Livingston on May 29, 2023, 18:15:00 UTC. Since it was a single detector event, it was poorly localised (Figure 4.1). The binary system has symmetric masses ($2.5 - 4.5 M_{\odot}$ and $1.2 - 2.0 M_{\odot}$, refer Table 4.1.1 for other parameters). The high probability of being an NSBH merger candidate implies that the primary mass lies in the mass gap between the most

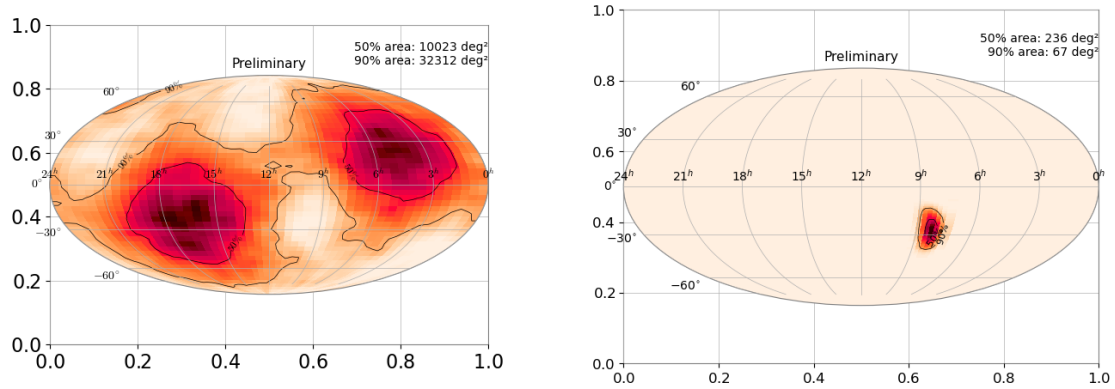

Figure 4.1: Bayestar sky location of GW230529 and S240422ed. Credit: GraceDB / LVK collaboration

massive NSs and the least massive BHs. Aside from the advantages of detecting an EM counterpart like for GW170817, understanding the mass gap objects will help us develop and constrain stellar evolution models. So far, no viable candidate has been detected in gamma (Lesage et al., 2023), X-ray (Waratkar et al., 2023; Sugita et al., 2023; Ronchini et al., 2024), optical wavelengths (Lipunov et al., 2023) or in neutrinos (IceCube Collaboration, 2023).

4.1.2 S240422ed

S240422ed was detected by LIGO-Hanford, LIGO-Livingston and *Virgo* on April 22, 2024, 21:35:13 UTC. This is reflected in the well-constrained sky map (Figure 4.1). S240422ed was initially predicted to be an NSBH system Ligo Scientific Collaboration et al., GCN 36236, and recently demoted as terrestrial Ligo Scientific Collaboration et al., GCN 36812. This is unfortunate given the constrained sky location that prompted multiple follow-up campaigns (Roberts & Fermi-GBM Team, 2024; Kuin et al., 2024; IceCube Collaboration, 2024), some proposing counterpart candidates in X-ray (Sun et al., 2024) and radio (Anumarlapudi et al., 2024), which were also discarded later as a background active galactic nuclei (AGN) activity (Levan et al., 2024). Multiple optical candidates were also discarded as un-

Parameter	**GW230529**	**S240422ed**
Primary mass $m_1/M_\odot$	$3.6^{+0.8}_{-1.2}$	$5.29^{+1.7}_{-2.86}$
Secondary mass $m_2/M_\odot$	$1.4^{+0.6}_{-0.2}$	$0.85^{+0.75}_{-0.19}$
Mass ratio $q = m_2/m_1$	$0.39^{+0.41}_{-0.12}$	$0.16^{+0.50}_{-0.06}$
Total mass $m/M_\odot$	$5.1^{+0.6}_{-0.6}$	$5.9^{+1.5}_{-1.9}$
Chirp mass $\mathcal{M}/M_\odot$	$1.94^{+0.04}_{-0.04}$	$1.715^{+0.004}_{-0.005}$
Redshift z	$0.04^{+0.02}_{-0.0}$	$0.04^{+0.02}_{-0.01}$
Detector-frame chirp mass $(1+z)\mathcal{M}/M_\odot$	$2.026^{+0.002}_{-0.002}$	$1.65^{+0.02}_{-0.03}$
Effective inspiral-spin parameter χ_{eff}	$-0.10^{+0.12}_{-0.17}$	$0.74^{+0.79}_{-0.69}$
Effective precessing-spin parameter χ_p	$0.40^{+0.39}_{-0.30}$	$0.37^{+0.58}_{-0.13}$
Luminosity distance D_L/Mpc	201^{+102}_{-96}	$187.3^{+74.52}_{-68.3}$

Table 4.1: Parameter estimation of O4 NSBH candidates in 90% credibility interval.

related (Piro et al., 2024; Piro, Simon, Polin, Coulter, Drout, Foley & Rojas-Bravo, S24; Ahumada et al., 2024). Nevertheless, we include the analysis for the signal with the last updated parameter estimation (Table 4.1.1) done under the assumption that it was of astrophysical origin.

4.2 Data reduction

We use TTEs from *Fermi*-GBM (2.4.2) and integrate the 128 energy channels of TTEs into 8 channels. Since we are searching for γ-ray signals modulated by the orbiting of the source, it is only logical that we transform the lightcurve in time to phase space. The orbital phase is obtained from Equation 3.8 as $\phi_{orbit} = \int_{-30s}^{t} \omega(x)dx|2\pi|$. The only variables here are the coalescence time (t_c) and the chirp mass ($\mathcal{M}$), which can be obtained from the GW event timing and parameter estimation respectively. Using the arrival times of TTEs, we rebin them in phase space. N_{bins} in phase space corresponds to I_k intervals:

$$I_k = \left\{ \left[0, \frac{2\pi}{N_{bins}}\right], \left[\frac{2\pi}{N_{bins}}, 2\frac{2\pi}{N_{bins}}\right], \ldots \left[(N_{bins}-1)\frac{2\pi}{N_{bins}}, 2\pi\right] \right\}$$

Analysing in time is the same as $N_{bins} = 1$ analysis in phase space. For background estimation, we assume a Poisson behaviour of the background. We estimate the rate for time windows of 100s, sliding over the duration of analysis (Goldstein et al., 2016). The results are interpolated and energy channels with high χ^2 are discarded. The background rates are then transformed into phase space. From Figure 4.2, it can be seen that higher N_{bins} increase the SNR.

4.3 Deriving the ranking statistic

As discussed earlier in Section 2.4, *Fermi*-GBM is triggered when the photon count rates exceed the background rates by in at least 2 NaI detectors in $50 - 300$ keV.

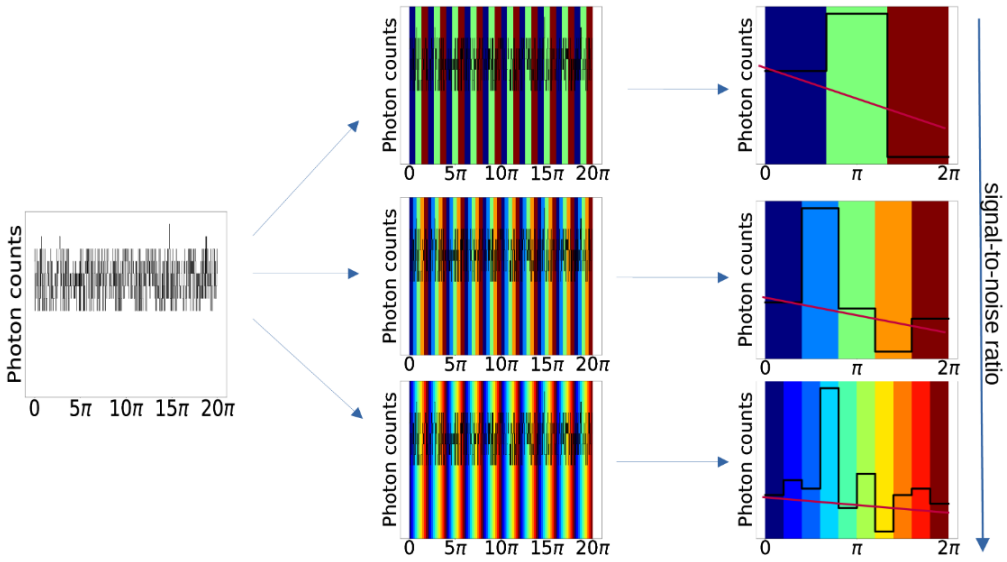

Figure 4.2: Illustrating the effect of the number of phase bins and intervals on the SNR

Generally, for a binning of 1.024 s, the threshold is 4.5σ above the background. However, the threshold can vary depending on the time window. For operational and scientific reasons, *Fermi* uses a sliding window ranging from 64 ms to 8.192 s, increasing by factors of 2. S22 proposed to instead examine the likelihood ratio combining signal and noise as:

$$\Lambda(d) = \frac{P(d|H_1)}{P(d|H_0)}, \tag{4.1}$$

where, $H1$ is the hypothesis of having signal (s), $H0$ is the hypothesis of having only noise (n), d is the data. Assuming, the signal amplitude s is the only variable, and the log-likelihood ratio (LLR) is obtained as $\mathcal{L}(d) = \ln \Lambda(d) = \ln \int \frac{P(d|H_1,s)}{P(d|H_0)} P(s) ds$.

We take the priors from Blackburn et al. (2015). For binned, uncorrelated Gaussian noise, the probability that the data has the signal, given prior knowledge s is,

$$P(d|H_1, s) = \prod_i \frac{1}{\sqrt{2\pi}\sigma_{d_i}} \exp\left(-\frac{(\tilde{d}_i - r_i s)^2}{2\sigma_{d_i}^2}\right), \tag{4.2}$$

and the probability that the data has only noise is given by,

$$P(d|H_0) = \prod_i \frac{1}{\sqrt{2\pi}\sigma_{n_i}} \exp\left(-\frac{\tilde{d}_i^2}{2\sigma_{n_i}^2}\right), \tag{4.3}$$

where, $\tilde{d}_i = d_i - \langle n_i \rangle$, i is the index referring to the pairs of detectors and energy channels and r is the detector response. The prior on the signal amplitude is given by Kocevski et al. (2018),

$$P(s) = \left[1 - \exp\left(-\left(\frac{s}{\gamma_{\rm prior}\sigma_{\ln\Lambda(d|s)}}\right)^{\beta_{\rm prior}}\right)\right] s^{-\beta_{\rm prior}}, \tag{4.4}$$

where $\gamma_{\rm prior} = 2.5$ and $\beta_{\rm prior} = 1$. Thus we arrive at the following equation for LLR that is almost Gaussian (Blackburn et al., 2013):

$$\begin{aligned}\mathcal{L}(d) = \ln\sigma_{\ln\Lambda(d|s)} + \ln\left[1 + \mathrm{erf}\left(\frac{s_{best}}{\sqrt{2}\sigma_{\ln\Lambda(d|s)}}\right)\right] + \ln\Lambda(d|s_{best}) \\ + \begin{cases} \ln\left[1 - \exp\left(-\frac{s_{\rm best}}{\gamma_{\rm prior}\sigma_{\ln\Lambda(d|s)}}\right)\right] - \beta_{\rm prior}\ln s_{\rm best} & \text{if } s_{\rm best} > 0 \\ -\beta_{\rm prior}\ln(\gamma_{\rm prior}\sigma_{\ln\Lambda(d|s)}) & \text{if } s_{\rm best} < 0, \end{cases}\end{aligned} \tag{4.5}$$

where, $\mathrm{erf}(x) = \frac{2}{\sqrt{\pi}}\int_0^x \exp(-t^2)dt$.

S22's `Python` program iterates over the parameters to maximise the LLR for a given trigger time t_c using Newton's method, which uses curvature information to optimise a value. Since the trigger time and the chirp mass are all subject to errors, a grid of values is created using the posteriors, and LLR is computed for each combination of time and mass. The values of LLR ≥ 5 are considered for further analysis. This cut-off, done to reduce computational costs, does not have any effect on the search sensitivity demonstrated in an earlier paper by Stachie et al. (2020) and in this thesis 4.4.1.

4.3.1 False alarm probability

We must evaluate the significance of the LLR for the given trigger t_c. The false alarm probability (FAP) is calculated by running the search for 1000 random times

(t_{rand}) in a window of a month centred on the trigger time and evaluating the probability of having a random event with LLR(t_{rand}) $\geq$ LLR(t_c). This could be from astrophysical sources such as solar flares or AGN activity, or it could be from detector noises. The search also excludes data collected when *Fermi* passes through the SAA (Section 2.4.2).

4.4 Targeted and chirp search

We conduct two searches: the GBM targeted search in time (Hereafter, targeted search (Goldstein et al., 2016)), and the chirp targeted search (Hereafter, chirp search) in phase space. We then evaluate the LLR and FAP for each search. S22 demonstrated the search sensitivity of these methods with injected signals and LVK-O3 NSBH and BNS candidates. As seen in Table 4.4.1, no significant candidates were identified. In the chirp search, GW170817 with the most symmetric component masses ($q = 0.4 - 1.0$) has the highest LLR, and GW190814 (Abbott et al., 2020) with the least symmetric component masses ($q \sim 0.1$) has the lowest LLR.

4.4.1 O4 results

The search as outlined above was conducted for NSBH candidates from LVK-O4. Figure 4.3 shows the distribution of FAP with respect to LLR of the background. As expected, the FAP decreases as the LLR. This observation also proves that the cut-off at LLR $\geq$ 5 does not exclude significant candidates as the FAP is close to 1. Table 4.4.1 summarises the maximum LLR obtained for our candidates and the corresponding FAP. Neither GW230529 nor S240422ed has a FAP value below the upper limit of 0.01. Comparing the astrophysical event GW230529 with 03 results, it does not follow the trend of mass symmetry and LLR.

Event	Chirp targeted search		Generic targeted search	
	LLR	**FAP**$^{+3\sigma}_{-3\sigma}$	**LLR**	**FAP**$^{+3\sigma}_{-3\sigma}$
GW170817	52.7	$0.034^{-0.021}_{+0.029}$	7.0	$0.554^{-0.064}_{+0.065}$
GW190425	26.9	$0.290^{-0.061}_{+0.062}$	7.2	$0.500^{-0.069}_{+0.065}$
GW190814	21.3	$0.135^{-0.044}_{+0.049}$	8.5	$0.217^{-0.055}_{+0.057}$
GW200105	25.4	$0.127^{-0.042}_{+0.048}$	10.7	$0.053^{-0.027}_{+0.033}$
GW200115	24.3	$0.237^{-0.057}_{+0.059}$	8.9	$0.168^{-0.047}_{+0.052}$

Table 4.2: LVK-03 results from S22.

Event	Chirp targeted search		Generic targeted search	
	LLR	**FAP**$^{+3\sigma}_{-3\sigma}$	**LLR**	**FAP**$^{+3\sigma}_{-3\sigma}$
GW230529	79.680	$0.186^{+0.052}_{-0.050}$	10.010	$0.279^{+0.063}_{-0.060}$
S240422ed	35.690	$0.222^{+0.056}_{-0.052}$	8.582	$0.295^{+0.064}_{-0.058}$

Table 4.3: LVK-O4 results from this work.

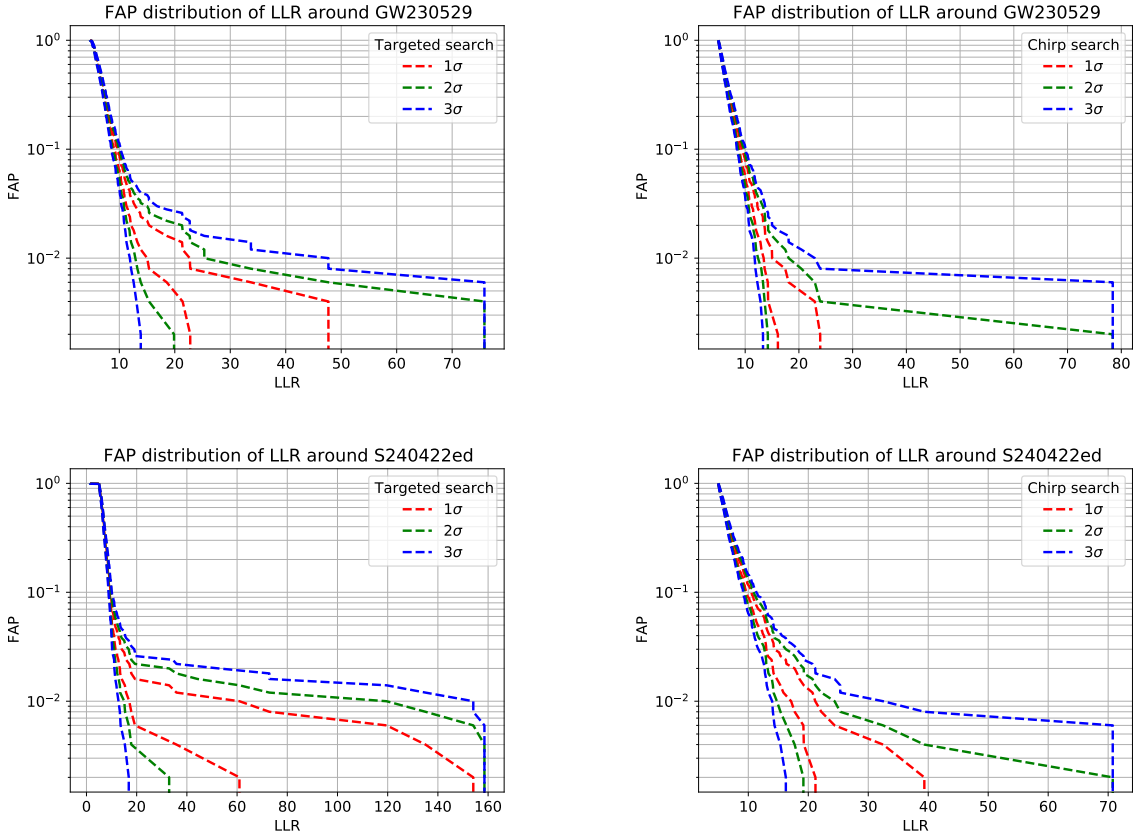

Figure 4.3: FAP distribution of LLR in a time window of 1 month around the two 04 NSBH events: GW230529 (top panel) and S240422ed (bottom panel). The generic targeted search (right) is compared with chirp search (left).

Chapter 5

Spectral lag estimation

Now, we shift our focus to the prompt emission. In this chapter, we describe the methodology to estimate spectral lag estimation. This work made use of the following software packages: `python` (Van Rossum & Drake, 2009), `gbm-data-tools` (Goldstein et al., 2022) `numpy` (Harris et al., 2020), `pandas` (Wes McKinney, 2010; pandas development team, 2024), and `matplotlib` (Hunter, 2007). Software citation information aggregated using `The Software Citation Station` (Wagg & Broekgaarden, 2024).

5.1 Data reduction

We first perform background reduction using the `Python` package `GBM Data Tools` (Goldstein et al., 2022). For a given GRB, we query continuous photon count TTEs (Section 2.4.1) from the GBM-burst catalogue hosted by HEASARC (Paciesas et al., 2012; von Kienlin et al., 2014; Narayana Bhat et al., 2016; von Kienlin et al., 2020). We use TTE for its higher time resolution. For the purpose of this work, we choose to use TTEs from a single detector with the highest SNR. Specifically, we choose among the NaI detectors for the energy range covered and better SNR compared

to the high-energy BGO detectors. NaI detectors cover an energy range of a few keV to 1 MeV and we integrate them into the four *Swift*-BAT energy bands: channel 1 ($15-25$ keV), 2 ($25-50$ keV), 3 ($50-100$ keV), and 4 ($100-200$ keV). This choice allows us to compare our results with existing literature on *Swift* GRBs. The lightcurves thus obtained by binning in time for 1.024 s. Visually inspecting the plot of the 1.024 s binned lightcurve, we choose two time intervals on either side of the burst to fit the background. A polynomial fit is performed and interpolated to obtain the background counts.

We need to obtain the reduced lightcurve for the chosen timescale of analysis. We rebin the original time-energy object to get the raw lightcurve. The background lightcurve is re-binned to the required timescale of analysis by redistributing the photon counts into each bin as shown in Equation 5.1. We assume this approximation has negligible effect since the background is almost linear.

$$N_B^{dt} = \frac{N_B^{1024} \times \mathrm{dt\ (s)}}{1.024(s)}, \tag{5.1}$$

and the uncertainty is,

$$\sigma(N_B^{dt}) = \frac{\sigma(N_B^{1024}) \times \mathrm{dt\ (s)}}{1.024(s)}, \tag{5.2}$$

where N_B^{dt} is the background counts in the timescale of analysis, dt, and N_B^{1024} is the background counts obtained by fitting 1.024s-binned lightcurve.

Now, the background can be subtracted as the timescales are same to get the signal counts: $N_S^{dt} = N_O^{dt} - N_B^{dt}$, where N_O^{dt} is the observed counts; The uncertainties are propagated as $\sigma(N_S^{dt}) = \sqrt{\sigma^2(N_O^{dt}) + \sigma^2(N_B^{dt})}$. Figure 5.1 shows the reduced lightcurve of GRB 211211A in the $100-300$ keV band and Figure 5.2 shows the energy spectrum. For each band, the SNR is obtained as shown in Equation 5.3, taking into account the variation in the observed counts and the background (Li & Ma, 1983).

$$\text{SNR} = \frac{N_S^{dt}}{\sigma(N_S^{dt})}. \tag{5.3}$$

5.2 Lag with cross-correlation

We compute spectral lag by calculating the discrete cross-correlation function (CCF), as shown in 5.4, between the HE counts $\{x_i\}$ and the LE counts $\{y_i\}$, and fitting the CCF to obtain the peak. The CCF is fit with a cubic polynomial of the form $\alpha x^3 + \beta x^2 + \gamma x + \delta = 0$ with a condition to be concave down ($\beta \leq 0$).

$$CCF = \frac{\sum_{i=1}^{N-d}(x_i - \overline{x}) \cdot (y_i - \overline{y})}{\sum_i (x_i - \overline{x})^2 \sum_i (y_i - \overline{y})^2}, \tag{5.4}$$

To estimate the lag with uncertainty, we employ bootstrapping as done by Norris et al. (2000). Bootstrapping is a resampling method applied to independent and identically distributed (i.i.d) random variables, that is employed when there is no knowledge of the 'true' error of a statistic of the parent population, here the lag of our lightcurves. We employed a standard bootstrap where we resampled the lightcurve uniformly and with replacement, and measured the lag of each such realisation. This resampling helps us rule out by-chance measurement of lags from noises or auto-correlation. We measure the lag of each realisation and the median of the distribution gives the central value. The uncertainties are reported in 68% confidence intervals. The original pipeline Norris et al. (2000) was in `IDL`, and we translated it to `Python` for its flexibility due to modular functions and widespread usage. Figure 5.3 represents the logic of the pipeline as a flowchart.

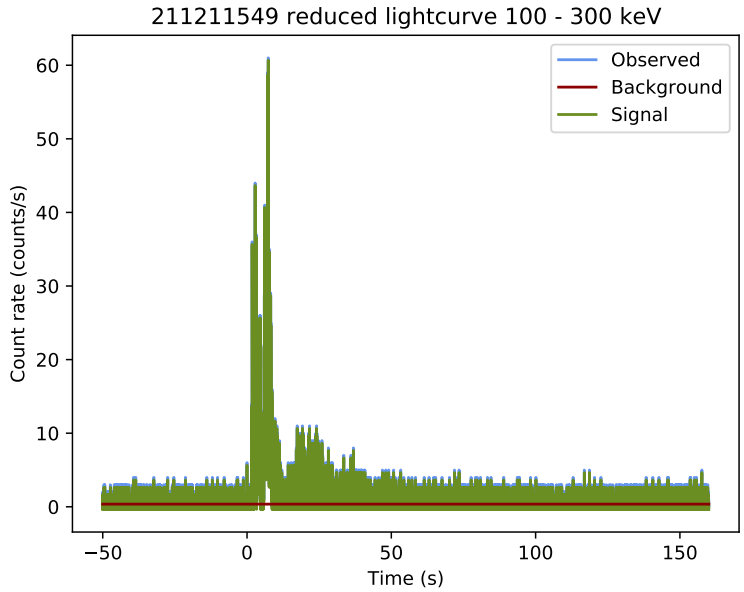

Figure 5.1: Reduced lightcurve (green) of GRB 211211A in 100 − 300 keV band. The background (red) and raw (blue) lightcurves are provided for comparison. The binning here is 1.024 s for better visualisation. Typically it is in the order of a few ms.

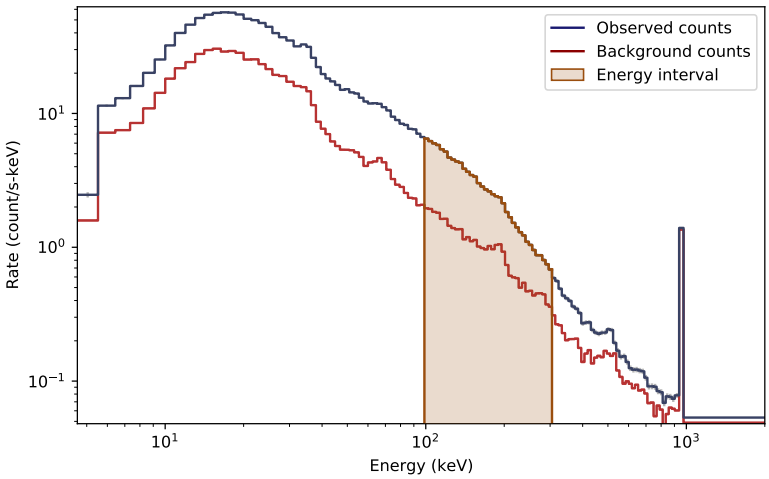

Figure 5.2: Energy spectrum of GRB 211211A. The spectrum of the background (red) and the raw counts (black). The selected region (orange) corresponds to the band 100 − 300 keV band. The SNR is 20.67

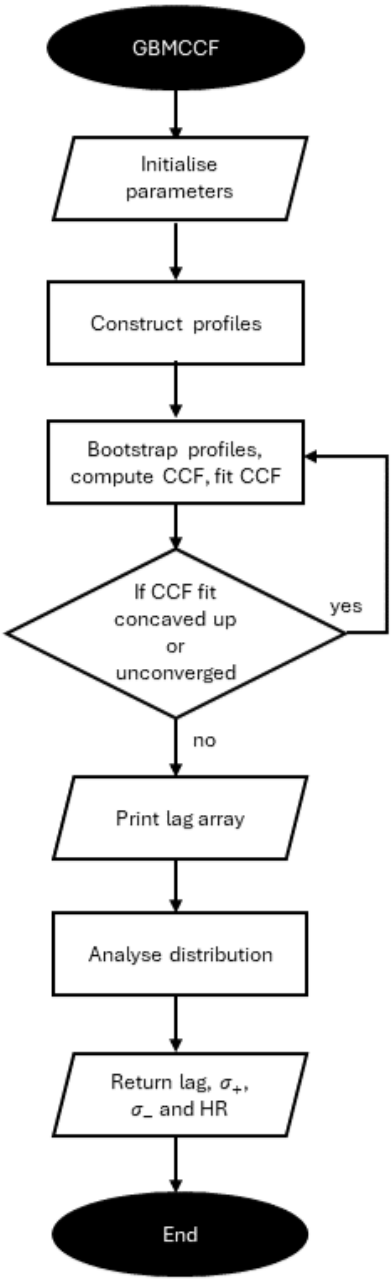

Figure 5.3: Flowchart of the spectral lag estimation pipeline

5.3 Results

5.3.1 Simulation

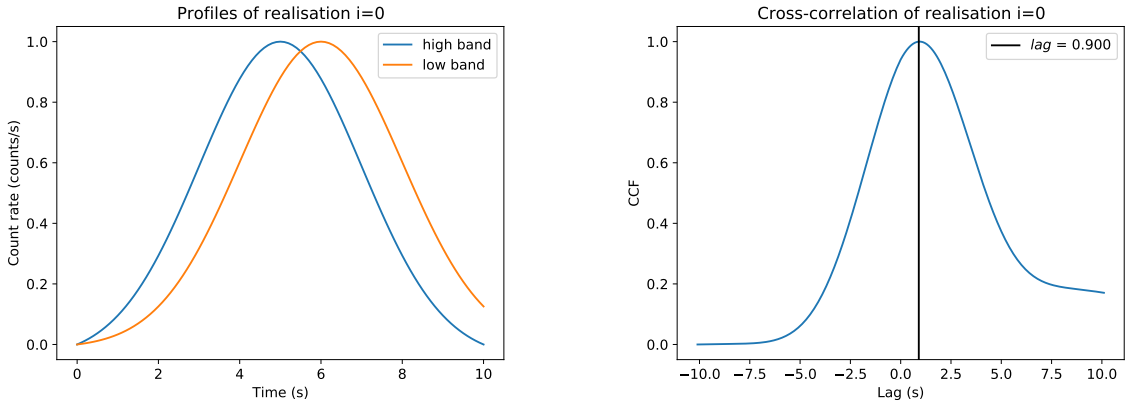

Figure 5.4: Simulation of a Gaussian pulse (left) and the respective CCF (right).

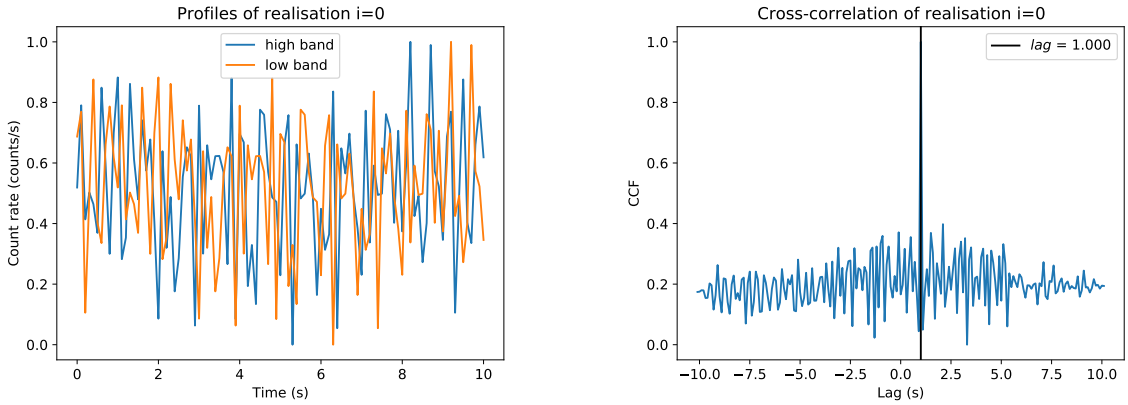

Figure 5.5: Simulation of a Gaussian noise (left) and the respective CCF (right).

Before applying the method to real data, we test it on simulated light curves. Figure 4.1 shows a Gaussian pulse, sampled at 0.1 s. The same pulse is shifted by 1 s for the second pulse. A lag of 1 s was retrieved for the original profile but the lag of all the bootstrapped realisations was zero. This is because bootstrapping requires that the two pulses should be i.i.d. Next, we simulate a lightcurve with each data

point chosen from a random Gaussian noise and produced two lightcurves with the same sampling and lag of $1.0^{+1.0}_{-0.7}$ s. We also perform a zero-test by correlating the same profile without any lag to check for the robustness of this method. The retrieved lag, as expected, was zero.

5.3.2 GRB 211211A

We chose a bright GRB to test our tool. Using multi-wavelength data, GRB 211211A was inferred to be produced by compact object merger (Troja et al., 2022). As discussed in Section 1, mergers are expected to produce short GRBs. The T_{90} duration from *Fermi* is 34.3 s (Mangan et al., 2021). This makes the GRB an interesting candidate to investigate the temporal lag behaviour. Table 5.3.2 summarises our results of lag in *Swift*-BAT energy bands: channel 1 ($15-25$ keV), 2 ($25-50$ keV), 3 ($50-100$ keV), and 4 ($100-200$ keV). A zero-test was performed by correlating the same channel. The lightcurves were binned at 2 ms and reduced as outlined in Section 5.1. For the analysis, we choose the main emission, and the time interval values are chosen such that the count rates at the particular times are comparable and closer to the background not to create offsets. As seen in Figure 5.8, our values coincide with *Swift* results for channels 3 and 1, from the original IDL program (Norris et al., 2000) and the literature Troja et al. (2022). Furthermore, we also see the trend of increasing lags with increasing energy separation between the bands. Taking the centroid of the bands, we obtain the plot in Figure 5.7. A linear fit is performed and a slope of 0.017 ms/keV was obtained.

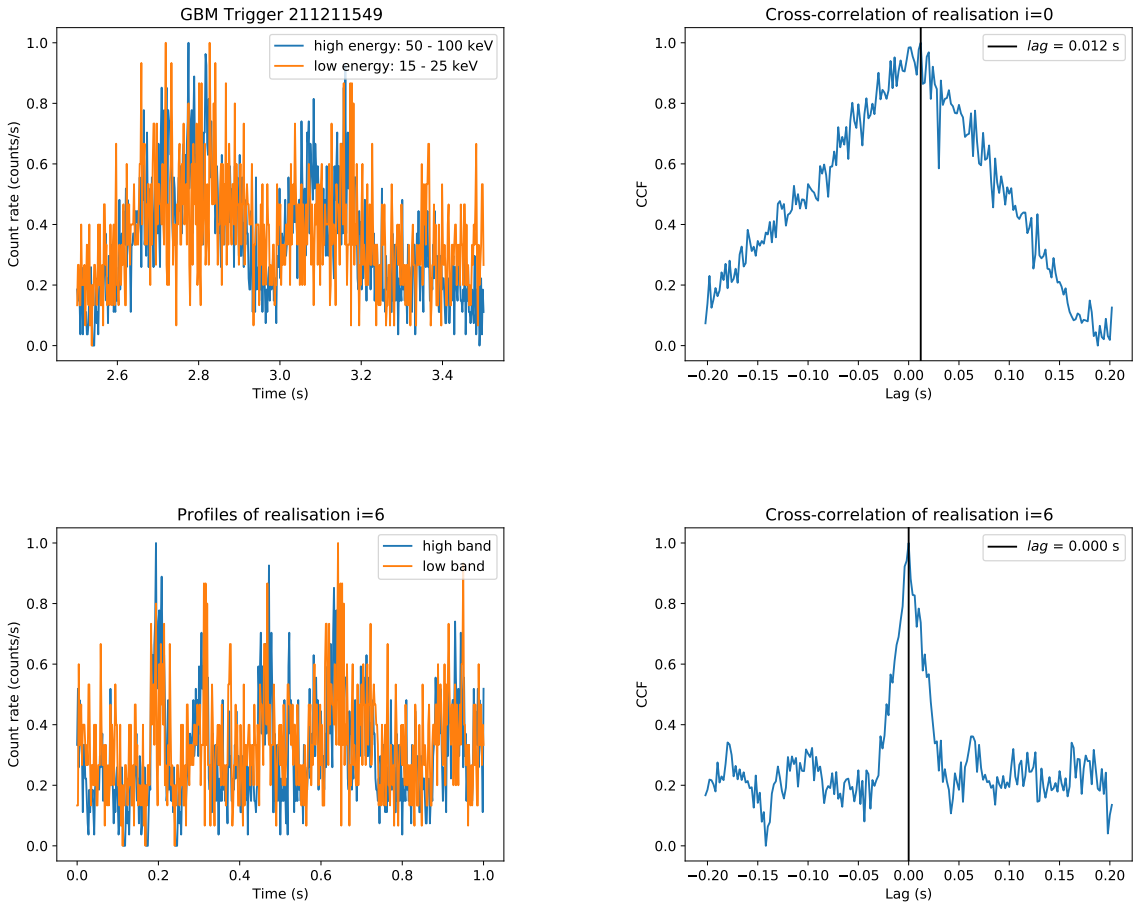

Figure 5.6: The top panel displays GRB 211211A lightcurve (left) and corresponding CCF (right). The bottom pannel shows the bootstrapped profile (left) and its CCF (right). The vertical black line marks the peak of the CCF.

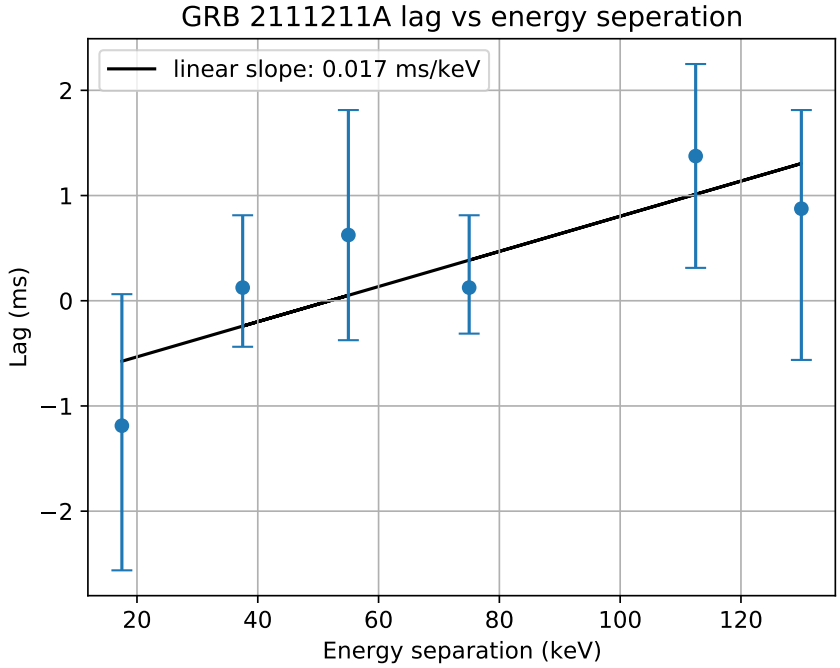

Figure 5.7: Comparison of lags obtained for GRB 211211A (blue points) vs the energy separation between the respective bands. The values are reported in Table 5.3.2

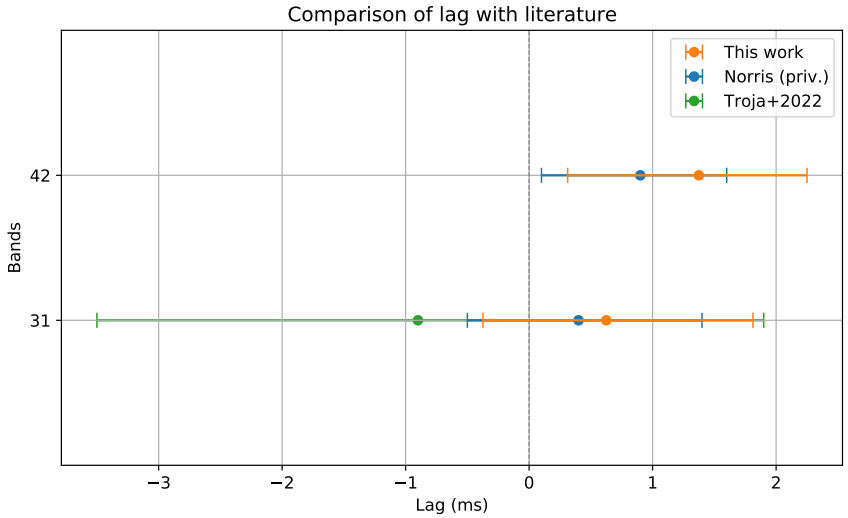

Figure 5.8: Comparison of lags obtained for GRB 211211A by our tool with *Fermi* (orange), compared to lag obtained for *Swift* lightcurves by Norris (private communication, blue) and reported in the literature (Troja et al., 2022) (green)

Band set	**Median lag** τ (ms)	σ_+ (ms)	σ_-
44	0	0	0
43	0.125	0.688	0.438
42	1.375	0.875	1.063
41	0.875	0.938	1.438
33	0	0	0
32	0.125	0.688	0.563
31	0.625	1.188	0.999
22	0	0	0
21	-1.187	1.250	1.375
11	0	0	0

Table 5.1: Lags obtained for *Fermi* GRB 211211549, binned at 2 ms, in *Swift*-BAT energy bands. The 1σ uncertainties are reported.

Source	**Band set**	**Median lag** τ (ms)	σ_+ (ms)	σ_-
This work	42	1.375	0.875	1.063
Norris (priv. comm.)	42	0.9	0.7	0.8
This work	31	0.625	1.188	0.999
Norris (priv. comm.)	31	0.4	1	0.9
Troja+2022	31	-0.9	2.8	2.6

Table 5.2: Comparison of our lag values for GRB 211211A with the literature.

Chapter 6

Conclusion

The two projects in this thesis are tied together by the overarching question: How can we better understand and classify GRBs in the context of multi-messenger astronomy, considering diverse emission properties and employing GW observations? The first part of the thesis focuses on possible emissions before the main GRB arising from the merger. To identify this premerger signal, we used the method S22 to transform the conventional targeted search in time into a 'chirp' search in phase space, by leveraging the GW parameters that we obtain from the orbital dynamics of the merging objects. Using a Bayesian approach, we conducted a sub-threshold search. We report non-detection of a significant precursor. In the second part of the thesis, we come to the prompt GRB emission. Despite the SGRB-merger association, there have been other evidences of a merger associated with an LGRB (or an SGRB with an extended emission) and failed collapsars producing SGRBs. So it is clear that the dichotomy based on duration might not always point to a progenitor. In looking for a new classification scheme, we realised the need for determined estimations of spectral lags. We provide a solution with a Python-based tool to provide rapid and well-constrained spectral lag estimations, primarily for *Fermi*-GBM GRBs. The tool uses a cross-correlation approach and bootstrapping for uncertainty estimation. We have demonstrated

the reliability of our tool, based on simulation and comparison with the literature of GRB 211211A. In a following paper, we aim to publish the results of a sample of bright GRBs and examine the application of spectral lag as a classification tool. To extend the analysis to fainter GRBs, the reduction pipeline needs to be tweaked to improve background reduction and achieve better SNR. The lag estimation pipeline is generic and could be applied to lightcurves from any observatories, such as *Swift* or the new *SVOM* after the lightcurve has been appropriately reduced. Having a rapid and uniform estimation of GRBs will allow us to peer deeper into the GRB physics such as constraining emission geometry, understanding central engine and radiation mechanisms, and systematically examining correlations like the lag-luminosity correlation. From the multi-messenger perspective, developing a timeline with the lags between different phases of emission, starting from GW to GRB, and even to neutrinos, will help us fully characterise the central engines of these energetic events and the emission and propagation of multi-messengers themselves.

6.1 Personal development and acknowledgements

This thesis has exposed me to the prospects of multi-messenger astronomy. We started with the spectral lag estimation as part of my internship at the University of Rome "Tor Vergata", Italy, with Eleonora Troja. Though I had worked in GRBs earlier, it was in optical wavelengths. From Nora and her postdoctoral researchers, I learned how to handle high-energy data and importantly, how to systematically investigate when there is a problem. I also learnt a simple but important lesson from Nora, which is to use a research notebook and write down the progress. I realised the necessity of this at the end of my thesis as I ran into the same problems again and I hadn't jotted it down thinking it was minor. A 15-minute presentation on the internship subject was presented in the winter school of the Erasmus Mundus MASS programme. We plan to expand this work to a larger sample size and publish it soon.

The second part of the thesis on precursors was conducted at the Observatory of Cote d'Azur, France, with Nelson Christensen. When I started the work, I experienced some hiccups due to the lack of expertise in big data searches and Bayesian approaches. I was unable to achieve the physical intuition and it felt like I was only seeing numbers. Thanks to Nelson's constant encouragement, I persevered with the goal of understanding these statistical methods and attained the results. A 3-minute presentation in the summer school of MASS. The two presentations have greatly improved my confidence in public speaking and the feedback has taught me how to make accessible talks. During this training, I also published a paper releasing the largest optical afterglow catalogue (Dainotti et al., 2024) and presented it in the 17th Marcel Grossmann meeting at Pescara, Italy. As the second author, it was challenging to handle the project alongside tackling the reviews and presentations for the paper. This experience highlighted soft skills I have to develop in a research career, like project management and organisation.

As I look forward to starting PhD in the fall of 2024, this experience has given me both the knowledge and soft skills required to start ahead. I want to thank my advisors and colleagues who were part of this amazing journey.

Scholarship Acknowledgement

Ridha Fathima Mohideen Malik acknowledges support through the Erasmus Mundus Joint Master (EMJM) scholarship funded by the European Union in the framework of the Erasmus+, Erasmus Mundus Joint Master in Astrophysics and Space Science – MASS. Views and opinions expressed are however those of the author(s) only and do not necessarily reflect those of the European Union or granting authority European Education and Culture Executive Agency (EACEA). Neither the European Union nor the granting authority can be held responsible for them.

Bibliography

Abac A. G., et al., 2024, , 970, L34

Abbott B. P., et al., 2016, , 116, 061102

Abbott B. P., et al., 2017a, , 119, 161101

Abbott B. P., et al., 2017b, , 551, 85

Abbott B. P., et al., 2017c, , 848, L13

Abbott R., et al., 2020, , 896, L44

Abdo A. A., et al., 2009, Astroparticle Physics, 32, 193

Acernese F., et al., 2015, Classical and Quantum Gravity, 32, 024001

Ahumada T., et al., 2024, GRB Coordinates Network, 36310, 1

Anumarlapudi A., Kaplan D., Dobie D., Murphy T., Lenc E., Ahumada T., 2024, GRB Coordinates Network, 36329, 1

Arcavi I., et al., 2017, , 551, 64

Ashton G., et al., 2019, , 241, 27

Atwood W. B., et al., 2009, , 697, 1071

Bailes M., et al., 2021, Nature Reviews Physics, 3, 344

Band D., et al., 1993, , 413, 281

Bernardini M. G., et al., 2015, , 446, 1129

Blackburn L., Briggs M. S., Camp J., Christensen N., Connaughton V., Jenke P., Veitch J., 2013, arXiv e-prints, p. arXiv:1303.2174

Blackburn L., Briggs M. S., Camp J., Christensen N., Connaughton V., Jenke P., Remillard R. A., Veitch J., 2015, , 217, 8

Blandford R. D., Znajek R. L., 1977, , 179, 433

Bromberg O., Nakar E., Piran T., Sari R., 2013, , 764, 179

Coulter D. A., et al., 2017, Science, 358, 1556

Dainotti M. G., et al., 2024, arXiv e-prints, p. arXiv:2405.02263

Dermer C. D., 1998, , 501, L157

Edvige Ravasio M., et al., 2023, arXiv e-prints, p. arXiv:2303.16223

Gehrels N., et al., 2004, , 611, 1005

Gehrels N., et al., 2006, , 444, 1044

Goldstein A., Burns E., Hamburg R., Connaughton V., Veres P., Briggs M. S., Hui C. M., The GBM-LIGO Collaboration 2016, arXiv e-prints, p. arXiv:1612.02395

Goldstein A., et al., 2017, , 848, L14

Goldstein A., Cleveland W. H., Kocevski D., 2022, Fermi GBM Data Tools: v1.1.1, (`https://fermi.gsfc.nasa.gov/ssc/data/analysis/gbm`)

Goodman J., 1986, , 308, L47

Hallinan G., et al., 2017, Science, 358, 1579

Harris C. R., et al., 2020, Nature, 585, 357

Horváth I., Balázs L. G., Bagoly Z., Ryde F., Mészáros A., 2006, , 447, 23

Hulse R. A., Taylor J. H., 1975, , 195, L51

Hulsman J., 2020, in den Herder J.-W. A., Nikzad S., Nakazawa K., eds, Society of Photo-Optical Instrumentation Engineers (SPIE) Conference Series Vol. 11444, Space Telescopes and Instrumentation 2020: Ultraviolet to Gamma Ray. p. 114442V (arXiv:2101.03084), doi:10.1117/12.2559374

Hunter J. D., 2007, Computing in Science & Engineering, 9, 90

IceCube Collaboration 2023, GRB Coordinates Network, 33980, 1

IceCube Collaboration 2024, GRB Coordinates Network, 36410, 1

Ioka K., Nakamura T., 2001, , 554, L163

Iyyani S., et al., 2013, , 433, 2739

Katz J. I., Canel L. M., 1996, , 471, 915

Kocevski D., Liang E., 2003, , 594, 385

Kocevski D., et al., 2018, , 862, 152

Kouveliotou C., Meegan C. A., Fishman G. J., Bhat N. P., Briggs M. S., Koshut T. M., Paciesas W. S., Pendleton G. N., 1993, , 413, L101

Kuin N. P. M., et al., 2024, GRB Coordinates Network, 36871, 1

Lesage S., Fermi-GBM Team GBM-LIGO/Virgo/KAGRA Group 2023, GRB Coordinates Network, 33892, 1

Levan A. J., Tanvir N. R., Steeghs D. T. H., Engrave Collaboration 2024, GRB Coordinates Network, 36325, 1

Li T. P., Ma Y. Q., 1983, , 272, 317

Li X. J., Zhang Z. B., Zhang X. L., Zhen H. Y., 2021, , 252, 16

Ligo Scientific Collaboration VIRGO Collaboration Kagra Collaboration 2024a, GRB Coordinates Network, 36236, 1

Ligo Scientific Collaboration VIRGO Collaboration Kagra Collaboration 2024b, GRB Coordinates Network, 36812, 1

Lipunov V. M., et al., 2017, , 850, L1

Lipunov V., et al., 2023, GRB Coordinates Network, 33895, 1

MAGIC Collaboration et al., 2019, , 575, 459

Maggiore M., 2007, Gravitational Waves. Vol. 1: Theory and Experiments. Oxford University Press, doi:10.1093/acprof:oso/9780198570745.001.0001

Mangan J., Dunwoody R., Meegan C., Fermi GBM Team 2021, GRB Coordinates Network, 31210, 1

McWilliams S. T., Levin J., 2011, , 742, 90

Meegan C., et al., 2009, , 702, 791

Mészáros P., Rees M. J., 1997, , 476, 232

Mészáros P., Kobayashi S., Razzaque S., Zhang B., 2004, Baltic Astronomy, 13, 317

Narayana Bhat P., et al., 2016, , 223, 28

Norris J. P., Nemiroff R. J., Bonnell J. T., Scargle J. D., Kouveliotou C., Paciesas W. S., Meegan C. A., Fishman G. J., 1996, , 459, 393

Norris J. P., Marani G. F., Bonnell J. T., 2000, , 534, 248

Paciesas W. S., et al., 1999, , 122, 465

Paciesas W. S., et al., 2012, , 199, 18

Paczynski B., 1986, , 308, L43

Piro A. L., Simon J. D., Polin A., Coulter D. A., Drout M. R., Foley R. J., Rojas-Bravo C., 2024, GRB Coordinates Network, 36275, 1

Rees M. J., Meszaros P., 1992, , 258, 41

Rees M. J., Meszaros P., 1994, , 430, L93

Roberts O. J., Fermi-GBM Team 2024, GRB Coordinates Network, 36241, 1

Ronchini S., et al., 2024, , 970, L20

Salmonson J. D., 2000, , 544, L115

Savchenko V., et al., 2017, , 848, L15

Schnittman J. D., Dal Canton T., Camp J., Tsang D., Kelly B. J., 2018, , 853, 123

Singer L. P., Price L. R., 2016, , 93, 024013

Soares-Santos M., et al., 2017, , 848, L16

Stachie C., et al., 2020, Classical and Quantum Gravity, 37, 175001

Stachie C., Dal Canton T., Christensen N., Bizouard M.-A., Briggs M., Burns E., Camp J., Coughlin M., 2022, , 930, 45

Sugita S., et al., 2023, GRB Coordinates Network, 33893, 1

Sun H., et al., 2024, GRB Coordinates Network, 36313, 1

Suvorov A. G., Kuan H.-J., Kokkotas K. D., 2024, arXiv e-prints, p. arXiv:2408.16283

Tanvir N. R., et al., 2017, , 848, L27

Taylor J. H., Fowler L. A., McCulloch P. M., 1979, , 277, 437

Troja E., Rosswog S., Gehrels N., 2010, , 723, 1711

Troja E., et al., 2017, , 551, 71

Troja E., et al., 2022, , 612, 228

Ukwatta T. N., et al., 2010, , 711, 1073

Ukwatta T. N., et al., 2012, , 419, 614

Valenti S., et al., 2017, , 848, L24

Van Rossum G., Drake F. L., 2009, Python 3 Reference Manual. CreateSpace, Scotts Valley, CA

Wagg T., Broekgaarden F. S., 2024, arXiv e-prints, p. arXiv:2406.04405

Wang J.-S., Peng Z.-K., Zou J.-H., Zhang B.-B., Zhang B., 2020, , 902, L42

Waratkar G., Bhalerao V., Bhattacharya D., Rao A. R., Vadawale S., AstroSat CZTI Collaboration 2023, GRB Coordinates Network, 33896, 1

Wei J., et al., 2016, arXiv e-prints, p. arXiv:1610.06892

Weisberg J. M., Taylor J. H., 1984, , 52, 1348

Wes McKinney 2010, in Stéfan van der Walt Jarrod Millman eds, Proceedings of the 9th Python in Science Conference. pp 56 – 61, doi:10.25080/Majora-92bf1922-00a

Zhang B., 2018, The Physics of Gamma-Ray Bursts, doi:10.1017/9781139226530.

Zhu S. J., 2015, PhD thesis, University of Maryland, College Park

pandas development team T., 2024, pandas-dev/pandas: Pandas, doi:10.5281/zenodo.10957263, (`https://doi.org/10.5281/zenodo.10957263`)

von Kienlin A., et al., 2014, , 211, 13

von Kienlin A., et al., 2020, , 893, 46